ESC-TR-2001-082

Quarterly Technical Report

Solid State Research

2002:2

Lincoln Laboratory

MASSACHUSETTS INSTITUTE OF TECHNOLOGY

LEXINGTON, MASSACHUSETTS

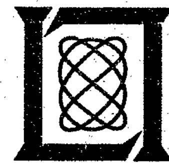

Prepared for the Department of the Air Force under Contract F19628-00-C-0002.

Approved for public release; distribution is unlimited.

20021008 018

This report is based on studies performed at Lincoln Laboratory, a center for research operated by Massachusetts Institute of Technology. The work was sponsored by the Department of the Air Force under Contract F19628-00-C-0002.

This report may be reproduced to satisfy needs of U.S. Government agencies.

The ESC Public Affairs Office has reviewed this report, and it is releasable to the National Technical Information Service, where it will be available to the general public, including foreign nationals.

This technical report has been reviewed and is approved for publication.

FOR THE COMMANDER

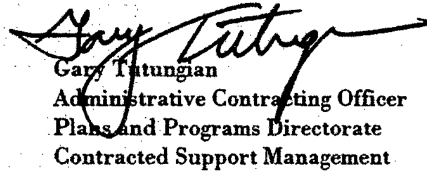

Gary Tutungian
Administrative Contracting Officer
Plans and Programs Directorate
Contracted Support Management

Non-Lincoln Recipients

PLEASE DO NOT RETURN

Permission is given to destroy this document when it is no longer needed.

Massachusetts Institute of Technology
Lincoln Laboratory

Solid State Research

Quarterly Technical Report

1 February — 30 April 2002

Issued 30 September 2002

Approved for public release; distribution is unlimited.

Lexington Massachusetts

ABSTRACT

This report covers in detail the research work of the Solid State Division at Lincoln Laboratory for the period 1 February through 30 April 2002. The topics covered are Quantum Electronics, Electro-optical Materials and Devices, Submicrometer Technology, Biosensor and Molecular Technologies, Advanced Imaging Technology, Analog Device Technology, and Advanced Silicon Technology. Funding is provided by several DoD organizations—including the Air Force, Army, DARPA, MDA, Navy, NSA, and OSD—and also by the DOE, NASA, and NIST.

TABLE OF CONTENTS

Abstract iii
List of Illustrations vii
List of Tables xi
Introduction xiii
Reports on Solid State Research xv
Organization xxiii

1. QUANTUM ELECTRONICS 1

    1.1 Wavelength Beam Combining of Mid-Infrared Semiconductor Lasers 1

2. ELECTRO-OPTICAL MATERIALS AND DEVICES 7

    2.1 Absorption Saturation Nonlinearity in InGaAs/InP p-i-n Photodiodes 7

3. SUBMICROMETER TECHNOLOGY 13

    3.1 Attenuating Phase-Shifting Mask at 157 nm 13
    3.2 Large-Area Patterning of ~50-nm Structures on Flexible Substrates Using Near-Field 193-nm Radiation 18

4. BIOSENSOR AND MOLECULAR TECHNOLOGIES 25

    4.1 Characterization and Detection Algorithm Development of the CANARY Sensor 25

5. ADVANCED IMAGING TECHNOLOGY 31

    5.1 Response of Molecular Beam Epitaxy–Passivated Back-Illuminated Charge-Coupled Devices to Low-Energy X Rays 31

6. ANALOG DEVICE TECHNOLOGY 35

6.1 Analog Array Processor for Cancellation of Undesired Signals in RF Front Ends 35

7. ADVANCED SILICON TECHNOLOGY 39

7.1 Microelectromechanical Systems Reliability Study 39

LIST OF ILLUSTRATIONS

Figure No.		Page
1-1	Photograph of optically pumped semiconductor laser (OPSL) module.	2
1-2	Wavelength beam combining optical configuration.	2
1-3	Spectrally dispersed image of OPSL facet.	3
1-4	Far-field divergence in beam combining dimension after output coupler.	4
1-5	Total output power and combined output power as a function of pump power per element. The beam combining efficiency is ~35%.	4
2-1	Cross section of large-area (300-μm diameter) photodiode with thick (3 μm) InGaAs absorption layer.	8
2-2	Top view of a fabricated photodiode.	9
2-3	Photodiode on TO-46-style header packaged and fiber pigtailed using laser welding.	9
2-4	Measurement, simulation, and simple model of integrated responsivity R_{INT} vs pulse energy E_P for two photodiodes: a Lincoln Laboratory device of 300-μm diameter and 3-μm thickness, and a commercial device of 50-μm diameter and 2-μm thickness. The beam diameter used for testing the 300-μm device was only 70 μm.	10
2-5	Comparison of the R_{INT} saturation response of two photodiodes: a Lincoln Laboratory 300-μm photodiode with $E_{SAT} \sim 20$ nJ (est.) and a commercial 50-μm photodiode with $E_{SAT} = 400$ pJ. The beam diameter used for testing the 300-μm device was 270 μm ($R = 90\%\ R_{MAX}$).	12
2-6	Two-tone third-order intermodulation-free dynamic range (IM3) tests of phase-encoded optical sampling system using (a) 50-μm and (b) 300-μm photodiodes.	12
3-1	Transmission intensity (solid line) and phase (dashed line) of the Pt layer at 157 nm as a function of thickness as predicted from measured optical constants of the film.	14
3-2	In situ 157-nm laser transmission of a Pt/spin-on-glass (SOG) bilayer as a function of incident dose. The incident fluence is 0.15 mJ/cm^2/pulse.	14

LIST OF ILLUSTRATIONS (Continued)

Figure No.		Page
3-3	Fabrication process flow of the bilayer SOG/Pt stack. PEB = postexposure bake; RIE = reactive ion etch.	16
3-4	(a) Scanning electron micrographs (SEMs) of 130-nm isolated spaces printed with the attenuating phase-shifting mask (APSM), through focus and for three doses; and (b) SEMs of dense 130-nm contact holes printed with the APSM, through focus and for three doses.	16
3-5	(a) Aerial image intensity slices taken at the resist surface when the chromeless phase-shifting mask is in perfect contact with the resist (see insert at top of figure). Shown separately are the intensity slices for s-polarized (parallel to page) and p-polarized (perpendicular to page) light. The exposure wavelength is 193 nm. (b) Image width at intensity = 0.2 as a function of mask-to-wafer gap derived from a compendium of intensity slices taken at the resist surface for simulations as a function of gap. These widths correspond to the expected resist width at an exposure dose ~2.5× the clearing dose, assuming a perfect threshold model of resist development. The actual linewidths will be dictated by resist characteristics. Our experiments used unpolarized light (solid black curve).	19
3-6	(a) Measured linewidths (symbols) for several commercial 193-nm resists as a function of exposure dose. The exposure doses were normalized to each resist's clearing dose so they could be plotted together. Exposures at doses $>2 \times E_0$ resulted in discontinuous resist lines. Vertical error bars are the range of values obtained over a 1-cm^2 field. Overlaid are the results (smooth curves) from Figure 3-5(a) where the simulated linewidths were tabulated at different intensity values. (b) Top-down electron micrographs of resist D taken at (top) 35-mJ/cm^2 and (bottom) 30-mJ/cm^2 exposure doses, where the average linewidths are 45 and 75 nm, respectively (E_0 = 15 mJ/cm^2). The four images at each dose are taken from different locations across the 1-cm^2 field.	20

LIST OF ILLUSTRATIONS (Continued)

Figure No.		Page
3-7	(a),(b) Top-down electron micrographs of resist D imaged on silicon following pattern transfer through 200 nm of organic undercoat. The final linewidths are ~75 nm. The pattern transfer was performed using a helicon oxygen plasma (P = 2 mTorr, power = 2500 W, flow = 200 sccm, bias = –50 V). (c) Electron micrograph image of resist D printed on 12.5-μm-thick polyimide after image transfer of the pattern 400 nm into the polyimide layer. The pattern transfer was performed using a reactive ion etcher (P = 15 mTorr, power = 150 W, flow = 200 sccm, bias = –150 V). The aspect ratio is ~5:1.	22
4-1.	Centrifugation format providing increased sensitivity and speed. Top: Photographs of centrifugation setup in (left) spinning (13,000 rpm) and (right) resting/measuring modes. Bottom: Plot of photon output produced by exposure of 25,000 B cells to 530,000 killed tularemia particles with and without centrifugation enhancement procedures as indicated in the schematic at right, where tularemia particles are represented by black circles and B cells by larger red circles.	26
4-2	Algorithm development.	27
4-3	Sensitivity of B-cell line specific for *Yersinia pestis*.	27
5-1	Oxygen x-ray response.	32
6-1	Power diverter. Inputs are A_1 and A_2. The angle θ is externally programmable.	36
6-2	Hardware demonstration of interference cancellation. $s(t)$ is the input with arbitrary normalized amplitude and phase, simulating the interference signal. The power diverters are programmed to perform rotations θ_1 and θ_2 as given by the equations at the lower right. The result is that in the output signals y the interference appears on one output channel only, and the other two channels are interference free and can be used to receive a desired signal that can be added to the input.	37
6-3	Photograph of the analog processing part of the bench-top demonstration.	37

LIST OF ILLUSTRATIONS (Continued)

Figure No. | | **Page**

Figure No.		Page
6-4	(a) Spectrum analyzer trace without any signal cancellation. Both a desired cw signal and a frequency modulated interferer are present. The interferer is completely masking the desired signal. (b) Output after the interference cancellation is turned on.	38
7-1	Scanning electron micrograph (SEM) of the MIT Lincoln Laboratory rf microelectromechanical systems (MEMS) capacitive switch.	40
7-2	Illustration of switch cycle test setup. A bipolar waveform was used to actuate the devices.	40
7-3	Measured switch capacitance in the up and down state after various numbers of switch cycles.	41
7-4	Hold down history for a MEMS capacitive switch showing dielectric charging and discharge. Values for times to release after failure are shown. The vertical dashed lines indicate pauses in the experiment with pause times as indicated.	43
7-5	Time to failure vs hold voltage for identical MEMS capacitive switches.	43
7-6	SEMS showing a tack point on a rf MEMS capacitive series switch. Close-up SEMs show a puck and divot at the tack point, indicating a strong surface bond at that point.	44

LIST OF TABLES

Table No.		Page
3-1	Comparison of Lithographic Results with Simulations for 130-nm Isolated Spaces	17
3-2	Comparison of Lithographic Results with Simulations for 130-nm Dense Contacts	17
4-1	CANARY False-Positive Rate	28
4-2	CANARY Sensitivity for *Francisella tularensis*	28
5-1	Oxygen X-Ray Peak Widths	33

INTRODUCTION

1. QUANTUM ELECTRONICS

Wavelength beam combining of eight broad-area, GaSb-based, optically pumped semiconductor lasers operating at $\lambda \sim 4$ μm has been demonstrated. The beam quality in the slow axis of the combined beam from eight laser elements was measured to be 10× the diffraction limit, which is the same beam quality as that of a single laser element, and the beam combining efficiency was ~35%.

2. ELECTRO-OPTICAL MATERIALS AND DEVICES

Agreement has been shown between measured nonlinear response and simulated absorption saturation for different absorber thickness in InGaAs/InP p-i-n photodiodes, providing strong evidence that the nonlinearity is due to absorption saturation. Devices with thicker absorber layers have been shown to be less nonlinear below the saturation energy, and the linearity of a photonic analog-to-digital converter has been improved by developing larger-area, thicker photodiodes.

3. SUBMICROMETER TECHNOLOGY

An attenuating phase-shifting mask, comprising a metal attenuator and transparent phase shifter, has been fabricated and tested at 157 nm. Increased depth of focus was demonstrated for 130-nm features, and the results were found to agree with numerical simulations.

Near-field contact exposures through a chromeless phase-shifting mask at 193 nm have been used to create arbitrarily shaped structures as small as 45 nm on thin (~10–15 μm) sheets of polyimide. Electromagnetic wave modeling using the finite difference time domain algorithm was used to model the near-field intensity distribution, and it predicted that exposure latitudes in excess of 15% are possible for printing isolated, semi-arbitrarily shaped features 50–60 nm wide.

4. BIOSENSOR AND MOLECULAR TECHNOLOGIES

Genetically engineered B-cell lines have been implemented as the key component of a novel sensor that provides robust, sensitive, and specific identification of pathogens in seconds. The reliable detection of low levels of pathogen has now been demonstrated, and a detection algorithm has been developed that yields a false-positive rate of <0.5%.

5. ADVANCED IMAGING TECHNOLOGY

The response of charge-coupled devices to low-energy x rays has been measured for detectors where the back-illuminated surface was passivated with a heavily doped *p*-Si layer grown by molecular beam epitaxy. The response was quite good, showing improved consistency in the width of the peak, compared to the previous process using ion implantation and conventional furnace annealing.

6. ANALOG DEVICE TECHNOLOGY

In many rf systems the dynamic range can be limited by large signals of either hostile or friendly origin that overload either the rf low-noise amplifier or the analog-to-digital converter, and in many situations the interference rejection is difficult even when the undesired signal is known. A new cancellation technique has been developed to address these difficult situations.

7. ADVANCED SILICON TECHNOLOGY

Reliability characterization has produced >10 billion switching cycles for a rf capacitive switch. The failure of capacitive switches due to charging while being held in the down state was investigated, and continuous hold down times of >80 days were measured; the time to failure is a strong function of the applied switching voltage, suggesting dielectric charging is a major factor in the failure mechanism.

REPORTS ON SOLID STATE RESEARCH
1 FEBRUARY THROUGH 30 APRIL 2002

PUBLICATIONS

Title	Authors	Publication
Ferrite Devices and Materials	J. D. Adam* L. E. Davis* G. F. Dionne E. F. Schloemann* S. N. Stitzer*	*IEEE Trans. Microw. Theory Tech.* **50**, 721 (2002)
RF Characterisation of Fully Depleted SOI MOSFET with Si Substrate Removed	C. L. Chen J. A. Burns K. Warner W. T. Beard*	*Electron. Lett.* **38**, 256 (2002)
Ion-Beam Processing Effects on the Thermal Conductivity of *n*-GaN/Sapphire (0001)	D. I. Florescu* F. H. Pollak* W. B. Lanford* F. Khan* I. Adesida* R. J. Molnar	*J. Appl. Phys.* **91**, 1277 (2002)
Nonlinear Dielectric Microwave Losses in MgO Substrates	M. A. Hein* D. E. Oates P. J. Hirst* R. G. Humphreys* A. V. Velichko*	*Appl. Phys. Lett.* **80**, 1007 (2002)
Characterization of Quartz Etched PSM Masks for KrF Lithography at the 100 nm Node	P. Rhyins* M. Fritze D. Chan* C. Carney* B. A. Blachowicz* M. Vieira* C. Mack*	*Proc. SPIE* **4562**, 486 (2002)

*Author not at Lincoln Laboratory.

PRESENTATIONS†

Title	Authors	Venue
Nonlinear Microwave Surface Impedance of YBCO Films: Latest Results and Present Understanding	D. E. Oates	Office of Naval Research Annual Review, Estes Park, Colorado, 13-16 February 2002
Optical Sampling for Analog-to-Digital Conversion	P. W. Juodawlkis	IEEE Lasers and Electro-Optics Society Chapter Meeting, Rome, New York, 28 February 2002
Overview of the MIT Lincoln Laboratory Electro-Optical Materials and Devices Group	J. C. Twichell	IEEE Lasers and Electro-Optics Society Chapter Meeting, Rome, New York, 28 February 2002
Recent Activities in the Electro-Optical Materials and Devices Group at MIT Lincoln Laboratory	J. C. Twichell P. W. Juodawlkis	IEEE Lasers and Electro-Optics Society Chapter Meeting, Rome, New York, 28 February 2002
Contamination Rates of Optical Surfaces at 157 nm in the Presence of Hydrocarbon Impurities	T. M. Bloomstein V. Liberman M. Rothschild S. T. Palmacci D. E. Hardy	SPIE Microlithography 2002, Santa Clara, California, 3-8 March 2002
Photospeed Considerations for Extreme Ultraviolet Lithography Resists	P. M. Dentinger* L. L. Hunter* D. J. O'Connell* S. Gunn* T. H. Fedynyshyn R. B. Goodman D. K. Astolfi	SPIE Microlithography 2002, Santa Clara, California, 3-8 March 2002

*Author not at Lincoln Laboratory.

† Titles of presentations are listed for information only. No copies are available for distribution.

Modeling of Acid Catalyzed Resists with Electron Beam Exposure	T. H. Fedynyshyn J. R. Gillman R. B. Goodman T. M. Lyszczarz S. J. Spector D. Lennon S. Deneault R. H. Bates*	SPIE Microlithography 2002, Santa Clara, California, 3-8 March 2002
High Resolution Fluorocarbon Resist for 157-nm Lithography	T. H. Fedynyshyn R. R. Kunz R. F. Sinta* M. Sworin W. A. Mowers R. B. Goodman	SPIE Microlithography 2002, Santa Clara, California, 3-8 March 2002
157 nm Pellicles: Polymer Design for Transparency and Lifetime	R. H. French* R. C. Wheland* W. Qiu* M. F. Lemon* G. S. Blackman* E. Zhang* J. Gordon* V. Liberman A. Grenville* R. Kunz M. Rothschild	SPIE Microlithography 2002, Santa Clara, California, 3-8 March 2002
Minimization of Image Placement Errors in Chromeless Phase-Shift Mask Lithography	M. Fritze B. Tyrrell	SPIE Microlithography 2002, Santa Clara, California, 3-8 March 2002
193 nm Lithography: Fundamentals and Issues (Short Course)	R. R. Kunz	SPIE Microlithography 2002, Santa Clara, California, 3-8 March 2002

*Author not at Lincoln Laboratory.

Spectroscopic Evaluation of Substrate Damage Caused by Focused Ion Beam Mask Repair for 157-nm Lithography	T. Liang* A. Stivers* G. Liu* G. Dao* V. Liberman M. Rothschild S. T. Palmacci L. Scipioni*	SPIE Microlithography 2002, Santa Clara, California, 3-8 March 2002
Long Term Durability Testing of Optical Coatings and Thin Films for 157-nm Lithography	V. Liberman M. Rothschild N. N. Efremow S. T. Palmacci J. H. C. Sedlacek A. Grenville*	SPIE Microlithography 2002, Santa Clara, California, 3-8 March 2002
Attenuating Phase-Shifting Mask at 157 nm	V. Liberman M. Rothschild S. J. Spector K. E. Krohn S. C. Cann S. Hein*	SPIE Microlithography 2002, Santa Clara, California, 3-8 March 2002
Resolution Enhancement of 157-nm Lithography by Liquid Immersion	M. Switkes M. Rothschild	SPIE Microlithography 2002, Santa Clara, California, 3-8 March 2002
Investigation of the Physical and Practical Limits of Dense-Only Phase Shift Lithography for Circuit Feature Definition	B. Tyrrell M. Fritze D. Yost D. Astolfi D. Chan* P. Rhyins*	SPIE Microlithography 2002, Santa Clara, California, 3-8 March 2002

*Author not at Lincoln Laboratory.

Title	Authors	Venue
CANARY B-Cell Sensor for Rapid Identification of Pathogens	F. Nargi M. Petrovick	Advanced Planning Briefing for Industry (APBI) Food Safety Workshop, Hunt Valley, Maryland, 7 March 2002
The Development of Recovery Techniques for Organisms and Nucleic Acids	M. A. Hollis	Gordon Research Conference: New Frontiers in Chemical and Biological Terrorism Defense, Harbortown, California, 10-15 March 2002
CANARY B-Cell Sensor for Rapid Identification of Pathogens	A. Young M. Petrovick	Gordon Research Conference: New Frontiers in Chemical and Biological Terrorism Defense, Harbortown, California, 10-15 March 2002
Thermal and Electronic Design Considerations for Wide-Bandgap Power Devices on Sapphire Substrates	C. Duffy R. Molnar R. A. Murphy Z. Lemnios	27th Annual Government Microcircuit Applications and Critical Technology (GOMACTech) Conference, Monterey, California, 11-14 March 2002
Intelligent RF Front End Study: Final Report	C. Keast L. Johnson A. Anderson G. Lyons M. Gouker J. Muldavin C-L. Chen	27th Annual GOMACTech Conference, Monterey, California, 11-14 March 2002
Relative Performance of Wide Bandgap Device Technology	R. Molnar C. Duffy* R. Murphy Z. Lemnios	27th Annual GOMACTech Conference, Monterey, California, 11-14 March 2002

*Author not at Lincoln Laboratory.

Basic Mechanisms Involved in Oxide Hardening by Ion Implantation	P. Gouker	20th Hardened Electronics and Radiation Technology (HEART) Conference, Monterey, California, 11-15 March 2002
Nanodot Materials and Devices in PbSnSeTe-Based Quantum Dot Superlattices	T. C. Harman P. J. Taylor M. P. Walsh B. E. LaForge G. W. Turner	ASM International Meeting, Seattle, Washington, 12 March 2002
Low-Voltage Modulators for Radio-Frequency Lightwave Integrated Circuits (RFLICS)	G. E. Betts P. J. Taylor D. C. Oakley J. P. Donnelly	DARPA RFLICS Program Review, Monterey, California, 12 March 2002
Optical Sampling for Analog-to-Digital Conversion	R. C. Williamson	IEEE Sarnoff Symposium, Princeton, New Jersey, 13 March 2002
Superconductive Quantum Computation: Moore's Law Meets Schrodinger's Cat	K. Berggren	Lasers and Quantum Electronics Seminar, Massachusetts Institute of Technology, Cambridge, Massachusetts, 13 March 2002
Orthogonal-Transfer Charge-Coupled Device Technology for WIYN (Wisconsin Indiana Yale NOAO) One-Degree Imager	B. E. Burke	One-Degree Imager Workshop, Tucson, Arizona, 18-19 March 2002
Lithography at Sub-100-nm Dimensions with Vacuum Ultraviolet Radiation	M. Rothschild	American Physical Society Meeting, Indianapolis, Indiana, 18-22 March 2002

Title	Authors	Venue
Charge-Coupled Device Focal Plane Array for the Chandra X-Ray Observatory	J. A. Gregory	American Vacuum Society, New England Chapter Meeting, Burlington, Massachusetts, 20 March 2002
Integrated Thermoelectric Material and Device Research	T. C. Harman P. J. Taylor W. D. Goodhue M. P. Walsh B. J. LaForge G. W. Turner	ONR/DARPA Thermoelectric Workshop, San Diego, California, 25 March 2002
Aerosol Triggers	T. H. Jeys	New England Bioterrorism Preparedness Workshop, MIT Lincoln Laboratory, Lexington, Massachusetts, 3-4 April 2002
Solid-State Focal Planes for Laser Radar Based on Geiger-Mode Avalanche Photodiodes Integrated with Digital CMOS Timing Circuits	B. F. Aull A. H. Loomis D. J. Young A. Stern B. J. Felton P. J. Daniels L. L. Retherford J. C. Aversa D. J. Landers	Military Sensing Symposia Specialty Group on Active EO Systems, MIT Lincoln Laboratory, Lexington, Massachusetts, 9-11 April 2002
Aerosol Triggers	T. H. Jeys	National Research Council, Washington, D.C., 15-16 April 2002
Biological Agent Warning Sensor (BAWS)	T. H. Jeys	National Research Council, Washington, D.C., 15-16 April 2002
High-Power Mid-Infrared Semiconductor Lasers	A. K. Goyal	Seminar, Massachusetts Institute of Technology, Cambridge, Massachusetts, 17 April 2002

Chandra X-Ray Observatory	J. A. Gregory B. E. Burke	Reception, Senate Russell Building, Washington, D.C., 24 April 2002
CANARY B-Cell Sensor for Rapid Identification of Pathogens	E. Schwoebel	Environmental Mutagen Society Meeting, Anchorage, Alaska, 27 April–2 May 2002
Biological Agent Warning Sensor (BAWS)	T. H. Jeys	Joint Service Calibration Group, Naval Surface Warfare Center, Bloomington, Indiana, 30 April 2002
Developing an Advanced BAWS	W. D. Herzog	Measurement and Signature Intelligence (MASINT) Biological Warfare Science and Technology Symposium, Monterey, California, 30 April–2 May 2002

ORGANIZATION

SOLID STATE DIVISION

D. C. Shaver, Head
R. W. Ralston, Associate Head
N. L. DeMeo, Jr., Assistant
Z. J. Lemnios, Senior Staff
J. W. Caunt, Assistant Staff
K. J. Challberg, Administrative Staff
J. D. Pendergast, Administrative Staff

SUBMICROMETER TECHNOLOGY

M. Rothschild, Leader
T. M. Lyszczarz, Assistant Leader
T. H. Fedynyshyn, Senior Staff
R. R. Kunz, Senior Staff

Astolfi, D. K.
Bloomstein, T. M.
Cann, S. G.
DiNatale, W. F.
Efremow, N. N., Jr.
Forte, A. R.
Geis, M. W.
Goodman, R. B.
Krohn, K. E.
Leibowitz, F. L.
Lennon, D. M.
Liberman, V.
Mowers, W. A.
Palmacci, S. T.
Sedlacek, J. H. C.
Spector, S. J.
Switkes, M.
Sworin, M.
Yoon, J. U.

QUANTUM ELECTRONICS

A. Sanchez-Rubio, Leader
T. Y. Fan, Assistant Leader
T. H. Jeys, Senior Staff
J. J. Zayhowski, Senior Staff

Aggarwal, R. L.
Augst, S. J.
Daneu, J. L.
Daneu, V.
Goyal, A. K.
Herzog, W. D.
Hybl, J. D.
Lynch, E. J.
O'Brien, P. W.
Ochoa, J. R.

ELECTRO-OPTICAL MATERIALS AND DEVICES

J. C. Twichell, Leader
G. W. Turner, Assistant Leader
D. L. Spears, Senior Staff
C. A. Wang, Senior Staff
R. C. Williamson, Senior Staff

Bailey, R. J.
Betts, G. E.
Calawa, D. R.
Calawa, S. D.
Connors, M. K.
Donnelly, J. P.
Goodhue, W. D.
Groves, S. H.
Hargreaves, J. J.
Harman, T. C.
Harris, C. T.
Huang, R. K.
Juodawlkis, P. W.
LaForge, B. E.
Liau, Z. L.
Mahoney, L. J.
Manfra, M. J.
McIntosh, K. A.
Missaggia, L. J.
Molnar, R. J.
Mull, D. E.
Napoleone, A.
Nitishin, P. M.
Oakley, D. C.
O'Donnell, F. J.
Plant, J. J.
Shiau, D. A.
Taylor, P. J.
Younger, R. D.

BIOSENSOR AND MOLECULAR TECHNOLOGIES

M. A. Hollis, Leader

Blanchard, D. J.
Filip, L. C.
Graves, C. A.
Harper, J. D.
Mathews, R. H.
Nargi, F. E.
Parameswaran, L.
Petrovick, M. S.
Postema-Zook, C. E.
Rider, T. H.
Schmidt, T. L.
Schwoebel, E. D.

ANALOG DEVICE TECHNOLOGY

T. C. L. G. Sollner, Leader
L. M. Johnson, Assistant Leader
A. C. Anderson, Senior Staff

Anthony, M. P.
Berggren, K. K.
Boisvert, R. R.
Fitch, G. L.
Kohler, E. J.
Lyons, W. G.
Macedo, E. M., Jr.
Murphy, P. G.
Oates, D. E.
Sage, J. P.
Santiago, D. D.
Seaver, M. M.
Slattery, R. L.
Weir, T. J.

ADVANCED IMAGING TECHNOLOGY

B. B. Kosicki, Leader
R. K. Reich, Assistant Leader
B. E. Burke, Senior Staff

Aull, B. F.
Ciampi, J. S.
Cooper, M. J.
Craig, D. M.
Daniels, P. J.
Doherty, C. L., Jr.
Dolat, V. S.
Felton, B. J.
Gregory, J. A.
Johnson, K. F.
Lind, T. A.
Loomis, A. H.
Mallen, R. D.
McGonagle, W. H.
O'Mara, D. M.
Osgood, R. M.
Percival, K. A.
Rathman, D. D.
Rose, M. K.
Stern, A.
Young, D. J.

ADVANCED SILICON TECHNOLOGY

C. L. Keast, Leader
V. Suntharalingam, Assistant Leader
P. W. Wyatt, Senior Staff

Austin, E. E.
Berger, R.
Bozler, C. O.
Burns, J. A.
Chen, C. K.
Chen, C. L.
D'Onofrio, R. P.
Fritze, M.
Gouker, P. M.
Healey, R. E.
Knecht, J. M.
Muldavin, J. B.
Newcomb, K. L.
Rabe, S.
Soares, A. M.
Travis, L.
Tyrrell, B. M.
Warner, K.
Wheeler, B. D.
Yost, D.-R.
Young, G. R.

1. QUANTUM ELECTRONICS

1.1 WAVELENGTH BEAM COMBINING OF MID-INFRARED SEMICONDUCTOR LASERS

Semiconductor lasers operating in the mid-infrared between $\lambda \sim 3$–$5\ \mu m$ are of interest for a variety of commercial and military applications. Some applications, such as infrared countermeasures, require multi-watt-class beams with near-diffraction-limited beam quality. Achieving such a high-brightness beam from a single semiconductor laser has proven to be challenging at any wavelength. To achieve this goal, we are pursuing the approach of wavelength beam combining (WBC) in which the optical power from an array of laser elements is spatially combined in such a way that the combined beam has the beam quality of a single element. In this way, the spatial brightness is scaled by the number of elements which make up an array. This is achieved by superimposing the beams from individual elements of a laser array, each operating at a different wavelength, both in the near field and far field by means of a dispersive element such as a diffraction grating [1]. WBC has already been applied to fiber lasers and diode lasers operating at $\lambda \sim 1\ \mu m$ [1] or $\lambda \sim 2\ \mu m$ [2],[3]. Here, we describe the application of WBC to an array of $\lambda \sim 4\ \mu m$, broad-area, optically pumped semiconductor lasers (OPSLs) [4].

The OPSLs are grown by solid-source molecular beam epitaxy on (100) *n*-GaSb substrates and are based on the integrated absorber design [5]. They are pumped using a $\lambda = 1.8\ \mu m$, InGaAs/InP diode array under pulsed conditions (35 μs, 2.5% duty cycle). The free-running wavelength for a 2-mm-long device is $\lambda \cong 3.95\ \mu m$ at an operating temperature of 78 K.

A photograph of the OPSL laser module is shown in Figure 1-1. The 2- by 8-mm bar is mounted epi-side-down onto a GaP heatspreader. The GaSb substrate is antireflection (AR) coated at the pump wavelength, and the laser output facet is AR coated. A GaP cylindrical microlens which nearly collimates the emission in the fast axis (perpendicular to the plane of the epilayers) is aligned to the facet and attached to the GaP heatspreader using uv-curing epoxy. The cylindrical GaP microlens is fabricated using the method of mass transport to have a focal length of ~100 μm [6], and both surfaces are AR coated. By bonding the GaP microlens to the GaP heatspreader, thermal-expansion-induced displacement of the microlens with respect to the laser facet is nulled. Even after many heating and cooling cycles between 300 and 78 K, no change in the microlens/laser alignment has been observed.

An array of OPSL elements is formed by imaging eight bars of the $\lambda = 1.8\ \mu m$ pump diode laser array onto the OPSL bar. The laser elements are spaced by ~500 μm and the pump stripe width is ~200 μm. For a single laser element the beam size times divergence product in the slow axis is 47 mm·mrad as measured at the full width at $1/e^2$ intensity points (fw$1/e^2$). This corresponds to ~10× the diffraction limit.

The OPSL module was cooled in a liquid nitrogen dewar and placed in the WBC configuration shown in Figure 1-2. The AR-coated Ge transform lens is placed one focal length away from both the OPSL array and the diffraction grating. The diffraction grating disperses the radiation in the slow dimension (in the plane of the epitaxial layers). The first-order diffracted beam is directed towards the

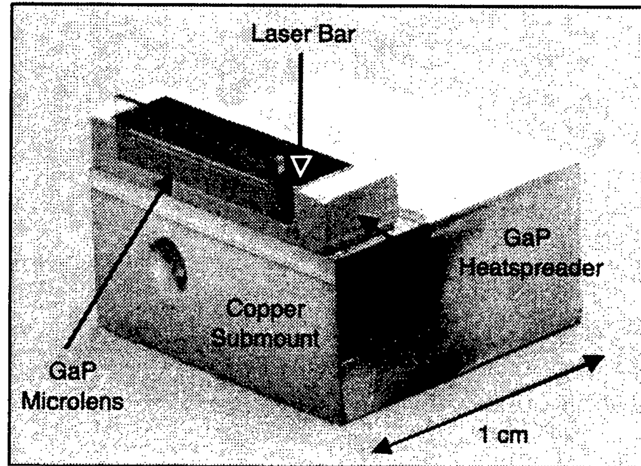

Figure 1-1. Photograph of optically pumped semiconductor laser (OPSL) module.

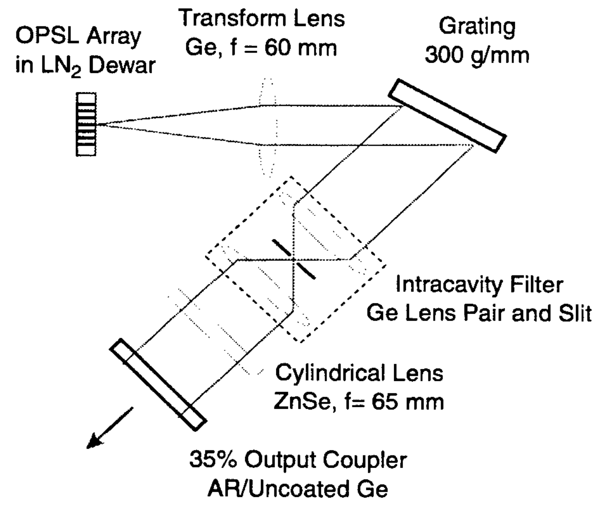

Figure 1-2. Wavelength beam combining optical configuration.

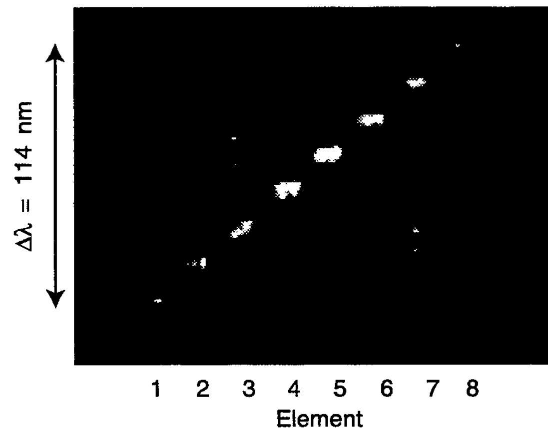

Figure 1-3. Spectrally dispersed image of OPSL facet.

uncoated surface of a Ge output coupler (R = 35%) to form an external cavity resonator. The ZnSe cylindrical lens placed between the grating and output coupler allows for compensation of astigmatism in the beams emitted from the microlensed laser module while the intracavity filter eliminates unwanted cross-coupling of laser elements. Under locked operation the wavelength of each laser element varies linearly with distance along the laser bar, and the far fields of the individual laser elements overlap after the output coupler.

Figure 1-3 shows a spectrally dispersed image of the OPSL array under wavelength-locked conditions. These were acquired by imaging the OPSL array at the plane of the microlens onto the input slit of a spectrometer and then imaging the output plane of the spectrometer using a Pt:Si focal plane array. In this way the lasing wavelength(s) of each of the individual laser elements are observed independently. As can be seen, the eight lasers that fall within a ~114-nm wavelength range are locked by the external cavity. As expected from the experimental configuration, the change in wavelength with position along the emitting aperture of the laser bar is $d\lambda/dx$ ~ 30 nm/mm. Figure 1-4 shows that the central far-field lobe for the combined beam after the output coupler has a width of 2.5 mrad fw$1/e^2$. Given that the near-field size is 20 mm fw$1/e^2$, the product of beam size and divergence is ~50 mm·mrad (~10× the diffraction limit), which is the beam quality of a single laser element.

The beam combining efficiency is defined here as the ratio of the combined power after the output coupler to the total power collected by the transform lens. Figure 1-5 plots both of these powers as a function of pump power per element. The beam combining efficiency is ~35%. By improving the quality of the AR facet coating on the OPSLs, to allow the use of a lower reflectivity output coupler, and by reducing intracavity losses, significantly higher beam combining efficiencies should be possible.

In summary, we have demonstrated WBC of eight broad-area OPSLs operating at λ ~ 4 μm. A technology was developed to attach GaP microlenses to these devices such that the micron-level alignment

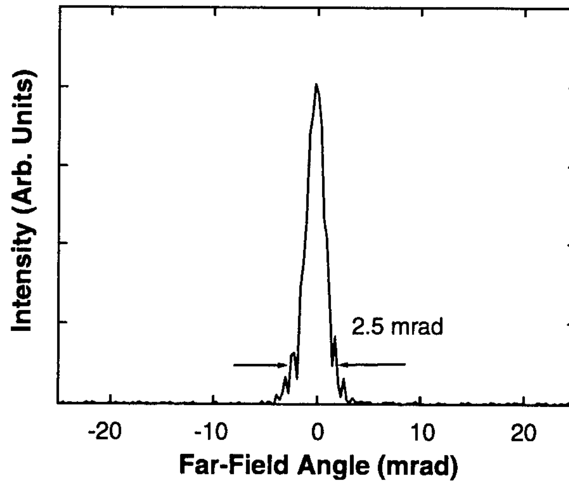

Figure 1-4. Far-field divergence in beam combining dimension after output coupler.

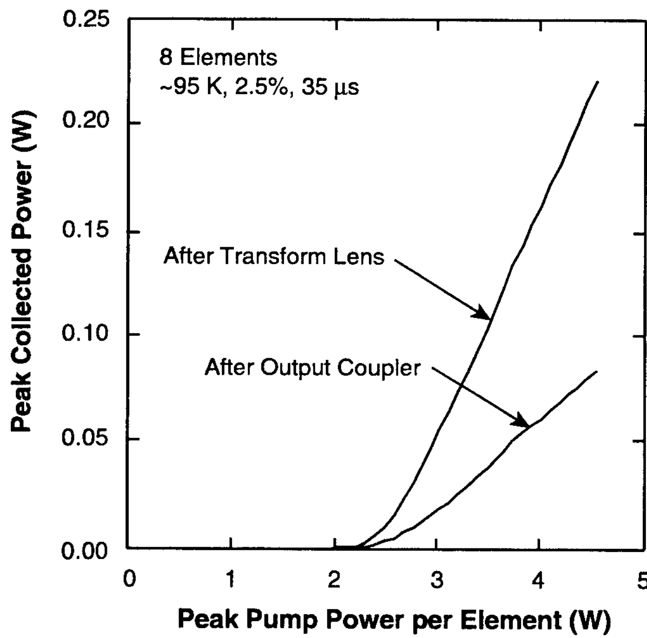

Figure 1-5. Total output power and combined output power as a function of pump power per element. The beam combining efficiency is ~35%.

tolerances are maintained as devices are cooled to liquid nitrogen temperatures. The beam quality of the combined beam in the slow axis of ~10× the diffraction limit was the same as that of a single laser element. The beam combining efficiency was ~35%. We are presently working towards increasing the beam combining efficiency by improving the quality of the AR facet coatings on the OPSLs and by reducing intracavity losses.

A. K. Goyal
A. Sanchez
G. W. Turner
T. Y. Fan
Z. L. Liau
M. J. Manfra
P. J. Foti
L. Missaggia
P. O'Brien
J. L. Daneu

REFERENCES

1. C. C. Cook and T. Y. Fan, in *Advanced Solid-State Lasers, OSA Trends in Optics and Photonics*, Vol. 26 of *Advanced Solid State Lasers*, M. M. Fejer, H. Injeyan, and U. Keller, eds. (Optical Society of America, Washington D.C., 1999), p. 163.

2. V. Daneu, A. Sanchez, T. Y. Fan, H. K. Choi, G. W. Turner, and C. C. Cook, *Opt. Lett.* **25**, 405 (2000).

3. W. A. Clarkson, V. Matera, T. M. J. Kendall, D. C. Hanna, J. Nilsson, and P. W. Turner, presented at the Conference on Lasers and Electro Optics and Quantum Electronics and Laser Science Conference, Baltimore, Md., 7-11 May 2001, paper CWM2.

4. A. K. Goyal, A. Sanchez, G. W. Turner, T. Y. Fan, Z. L. Liau, M. J. Manfra, P. J. Foti, L. Missaggia, P. O'Brien, and J. L. Daneu, presented at the Conference on Lasers and Electro Optics and Quantum Electronics and Laser Science Conference, Baltimore, Md., 7-11 May 2001, paper WQ3.

5. H. K. Choi, A. K. Goyal, S. C. Buchter, G. W. Turner, M. J. Manfra, and S. D. Calawa, presented at the Conference on Lasers and Electro Optics and Quantum Electronics and Laser Science Conference, San Francisco, Calif., 7-12 May 2000, paper CMM42.

6. Z. L. Liau, D. Z. Tsang, and J. N. Walpole, *IEEE J. Quantum Electron.* **33**, 457 (1997).

2. ELECTRO-OPTICAL MATERIALS AND DEVICES

2.1 ABSORPTION SATURATION NONLINEARITY IN InGaAs/InP p-i-n PHOTODIODES

Photodiode nonlinearities have been shown to degrade the performance of analog optical links and signal processing systems [1],[2]. The reported work to understand and reduce these nonlinearities has focused primarily on the nonlinearity due to electric field screening induced by the photogenerated carriers [3],[4]. This space-charge field screening decreases the carrier drift velocity, reducing the photodiode bandwidth. Recently, there has been interest in using picosecond optical pulses to sample analog electrical signals in photonic analog-to-digital converters (ADCs) [5]. The high carrier densities generated by these short pulses during photodetection can cause absorption saturation ("bleaching"), which reduces the photodiode's responsivity.

Here, we present measured and simulated results that support the observation of a photodiode nonlinearity due to absorption saturation. We compare the pulsed nonlinear response of two InGaAs/InP mesa-etched p-i-n photodiodes: a commercial 50-μm-diam device having a 1-μm-thick InGaAs absorbing layer, and a custom device that was developed at Lincoln Laboratory having a 300-μm diameter and a 3-μm-thick InGaAs absorbing layer. We demonstrate that the high linearity of the 300-μm-diam photodiodes greatly improves the linearity of an optically sampled ADC.

The top-illuminated, ring-contact custom photodiode was grown via organometallic vapor-phase epitaxy (OMVPE). The material structure, shown in Figure 2-1, was grown on an n^+ (001) InP substrate and contains the following layers: an n-InP buffer layer (0.5 μm), a nominally undoped InGaAs absorbing layer (3 μm), a p-InP cap layer (0.5 μm), and a p^+ InGaAs contact layer (20 nm). The InGaAs/InP heterojunctions are not graded. The device uses a mesa-etched design to minimize the slow diffusive photocurrent tails that have been observed in planar photodiode structures. The InGaAs contact layer was removed from the optical window, and the surface was antireflection coated to maximize the responsivity. Figure 2-2 shows a top view of a fabricated photodiode. These photodiodes, shown in Figure 2-3, were the first Lincoln-built devices packaged using the recently acquired Newport laser-welding fiber-pigtailing facility. The maximum responsivity at 1550 nm was 1.1 A/W (90% external efficiency). The photodiode exhibited low dark current (5 nA at 10-V bias), high reverse breakdown voltage (>50 V), and a capacitance of 4 pF.

We define the integrated responsivity R_{INT} for pulsed excitation as the ratio of the total charge Q output from the photodiode to the energy E_{P} of the input optical pulse. The nonlinear dependence of R_{INT} on E_{P} was investigated by simulating the propagation of an optical pulse through an InGaAs absorbing layer. The quantum efficiency was computed by assuming that every absorbed photon results in an output charge carrier. The propagation simulation is based on the following equations:

$$\frac{dI_{\mathrm{P}}(z,t)}{dz} = -\alpha\,(N)\,I_{\mathrm{P}}(z,t) \tag{2.1}$$

$$\frac{dN(z,t)}{dt} = \frac{\alpha\,[N(z,t)]\,I_{\mathrm{P}}(z,t)}{h\nu} - \frac{N(z,t)}{\tau_{\mathrm{C}}} \quad (2.2)$$

$$\alpha\,(N) = \alpha_0 \left(1 - \frac{N}{N_{\mathrm{SAT}}}\right) \quad (2.3)$$

where N is the carrier density, I_{P} is the temporal Gaussian pulse intensity profile, h is Planck's constant, ν is the optical frequency, τ_{C} is the effective carrier lifetime, $\alpha(N)$ is the carrier dependent absorption coefficient, a_0 is the linear absorption coefficient, and N_{SAT} is the saturation carrier density. The amplitude of the input I_{P} profile was defined by approximating the spatial Gaussian beam profile as a uniform distribution over the area defined by the $1/e$ beam radius.

The simulation parameters are based on known or measured quantities, and the only adjustable fitting parameter is the beam radius. The parameter values used are $\alpha_0 = 7700$ cm^{-1} as computed from the measured responsivity; $\tau_{\mathrm{C}} = 1$ ns; $\tau_{\mathrm{P}} = 30$ ps, which equals the full width at half-maximum optical pulse width; and $N_{\mathrm{SAT}} = 1.2 \times 10^{18}$ cm^{-3}. The exact value of τ_{C} is not critical since it is much larger than τ_{P}, implying that photogenerated carriers are not removed during the pulse propagation. The large value of τ_{C} is consistent with the slow sweep out due to field screening at high carrier densities [6]. The absorber thickness L was either 1 or 3 μm depending on the device being simulated.

Measurements of R_{INT} vs E_{P} were performed using 30-ps optical pulses generated by a mode-locked fiber ring laser (60-MHz rate, $\lambda = 1550$ nm) and amplified using an erbium-doped fiber amplifier (EDFA).

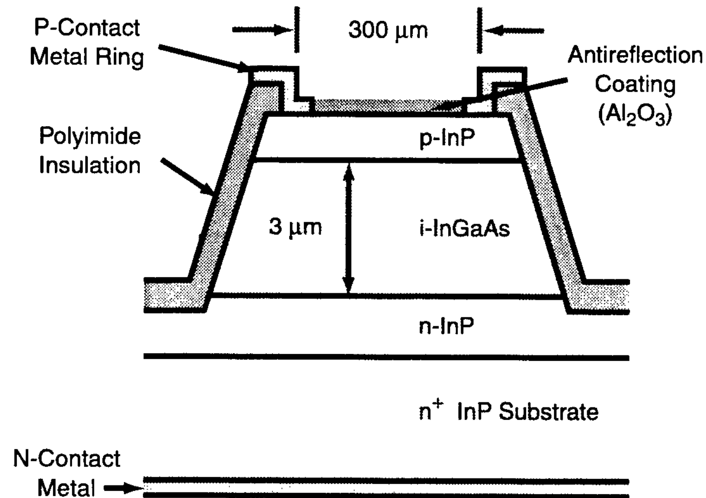

Figure 2-1. Cross section of large-area (300-μm diameter) photodiode with thick (3 μm) InGaAs absorption layer.

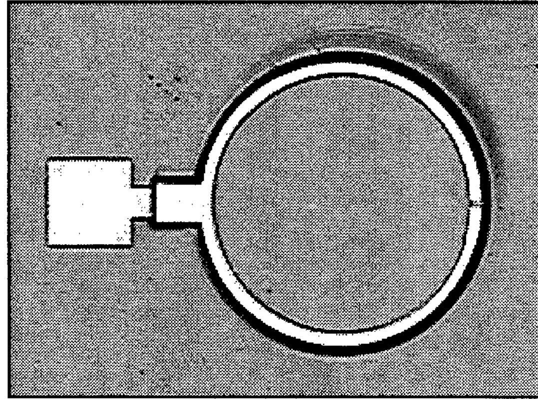

Figure 2-2. Top view of a fabricated photodiode.

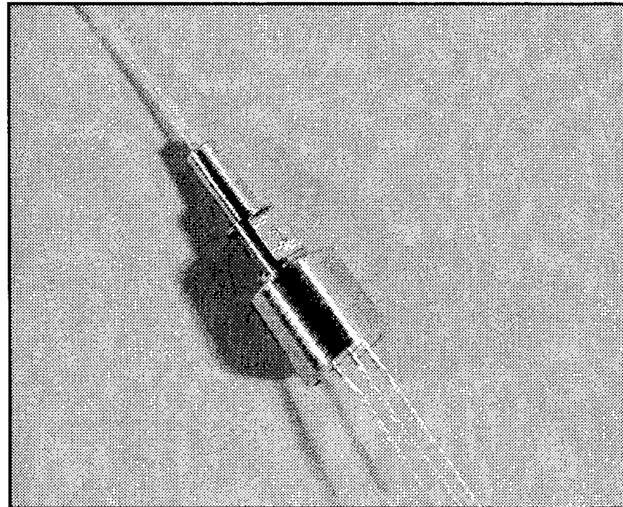

Figure 2-3. Photodiode on TO-46-style header packaged and fiber pigtailed using laser welding.

The pulse energy was varied via an optical attenuator following the EDFA. The optical power at the photodiode input was measured using a power meter, and the output current was measured using a dc current meter. R_{INT} was computed as the ratio of the average optical power to the dc current.

Figure 2-4 shows the measured and simulated values of R_{INT} vs E_P for the two photodiode structures. To allow the responsivity nonlinearity to be observed in the 300-μm device, the input optical fiber was positioned so that the $1/e$ beam diameter at the photodiode was only 70 μm. Note the excellent

agreement between the measured and simulated data. Also shown are the least-squares fits of the data to the approximate expression

$$R_{\mathrm{INT}}(E_{\mathrm{P}}) = \frac{R_0}{1+\left(E_{\mathrm{P}}/E_{\mathrm{SAT}}\right)} \tag{2.4}$$

where R_0 is the linear responsivity and E_{SAT} is the saturation pulse energy. The fit is good for the 1-μm-thick absorber (R_0 = 0.74 A/W, E_{SAT} = 410 pJ), but not for the 3-μm-thick absorber (R_0 = 1.03 A/W, E_{SAT} = 22 nJ) where R_{INT} is less nonlinear at low E_{P} and then saturates more abruptly.

On a different large-area device, the input fiber was positioned to slightly overfill the 300-μm aperture (beam diameter = 270 μm, R = 90% R_{MAX}). As shown in Figure 2-5, for this alignment no nonlinearity was observed for E_{P} as large as 1 nJ, the value at which the device failed due to excess current flow. The simulated 300-μm curve uses the same parameters as the 70-μm-beam simulation in Figure 2-4, except that the diameter was increased by a factor of 3.9. Note that R_{INT} of the 50-μm device, repeated in Figure 2-5 for comparison, is highly nonlinear at the typical value of E_{P} used for optical sampling (20–30 pJ).

The impact of photodiode linearity on the linearity of the phase-encoded optical sampling technique [5] was evaluated by measuring the two-tone third-order intermodulation-free dynamic range (IM3).

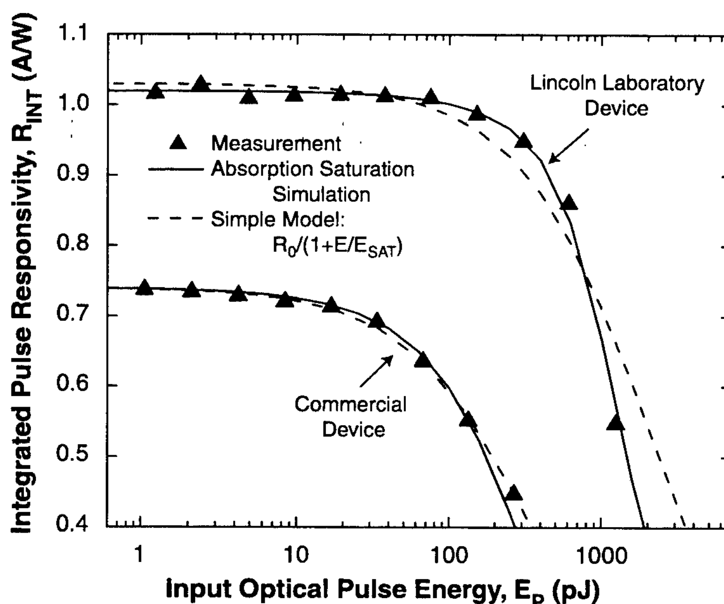

Figure 2-4. Measurement, simulation, and simple model of integrated responsivity R_{INT} vs pulse energy E_P for two photodiodes: a Lincoln Laboratory device of 300-μm diameter and 3-μm thickness, and a commercial device of 50-μm diameter and 2-μm thickness. The beam diameter used for testing the 300-μm device was only 70 μm.

Phase-encoded sampling reduces the Mach-Zehnder sampling modulator nonlinearity to the point where the photodiode nonlinearity dominates. Integrate-and-reset detection was used so that the only photodiode nonlinearity that affected the sampling linearity was the R_{INT} nonlinearity. In the measurements, the modulation index ($m = V_{IN,PP}/V_{\pi}$) for each tone was 15%, and the average E_P was 20 pJ. Use of the larger, thicker photodiode structure improved the IM3 by 17 dB, as shown in Figure 2-6. If the linearity were limited by the photodiodes only, the IM3 should have increased by more than 40 dB. The smaller observed improvement indicates that other factors (e.g., amplifier nonlinearity, residual calibration errors) limit the linearity when the 300-μm photodiodes are used.

In summary, the agreement between the measured nonlinear response and the absorption saturation simulation for different absorber thickness provides strong evidence that the R_{INT} nonlinearity is due to absorption saturation. Another possible cause of the decrease in R_{INT} is carrier recombination in the screened-field region during the long, pulse-energy-dependent carrier-sweep-out period. However, it is not likely that the physics of the carrier recombination nonlinearity would be accurately modeled by the absorption-saturation equations used here. We have also shown that devices having thicker absorber layers are less nonlinear below the saturation energy. We have improved the linearity of a photonic ADC by developing larger-area, thicker photodiodes. Recent analyses indicate that reduced photodiode nonlinearity may also improve the accuracy and stability of the calibration techniques used in time-interleaved photonic ADCs.

P. W. Juodawlkis, F. J. O'Donnell, J. J. Hargreaves
D. C. Oakley, A. Napoleone, S. H. Groves
L. J. Mahoney, K. M. Molvar, L. J. Missaggia
J. P. Donnelly, R. C. Williamson, J. C. Twichell

REFERENCES

1. K. J. Williams, L. T. Nichols, and R. D. Esman, *IEEE J. Lightwave Technol.* **16**, 192 (1998).

2. D. C. Scott, T. A. Vang, J. Elliott, D. Forbes, J. Lacey, K. Everett, F. Alvarez, R. Johnson, A. Krispin, J. Brock, L. Lembo, H. Jiang, D. S. Shin, J. T. Zhu, and P. K. L. Yu, *IEEE Photon. Technol. Lett.* **12**, 422 (2000).

3. P.-L. Liu, K. J. Williams, M. Y. Frankel, and R. D. Esman, *IEEE Trans. Microwave Theory Tech.* **47**, 1297 (1999).

4. Y.-L. Huang and C.-K. Sun, *IEEE J. Lightwave Technol.* **18**, 203 (2000).

5. P. W. Juodawlkis, J. C. Twichell, G. E. Betts, J. J. Hargreaves, R. D. Younger, J. L. Wasserman, F. J. O'Donnell, K. G. Ray, and R. C. Williamson, *IEEE Trans. Microwave Theory Tech.* **49**, 1840 (2001).

6. P. W. Juodawlkis, J. J. Hargreaves, and J. C. Twichell, *Proceedings of the Conference on Lasers and Electro Optics* (Optical Society of America, Washington, D.C., 2002), p. 11.

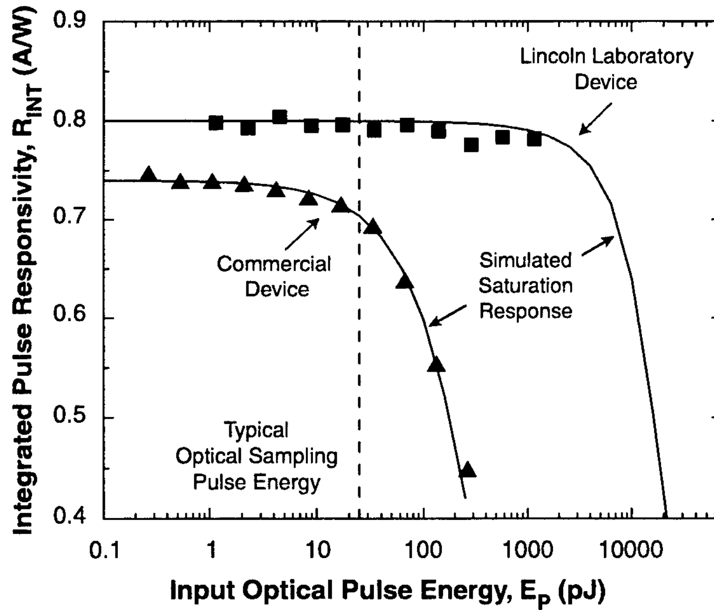

Figure 2-5. Comparison of the R_{INT} saturation response of two photodiodes: a Lincoln Laboratory 300-μm photodiode with E_{SAT} ~ 20 nJ (est.) and a commercial 50-μm photodiode with E_{SAT} = 400 pJ. The beam diameter used for testing the 300-μm device was 270 μm (R = 90% R_{MAX}).

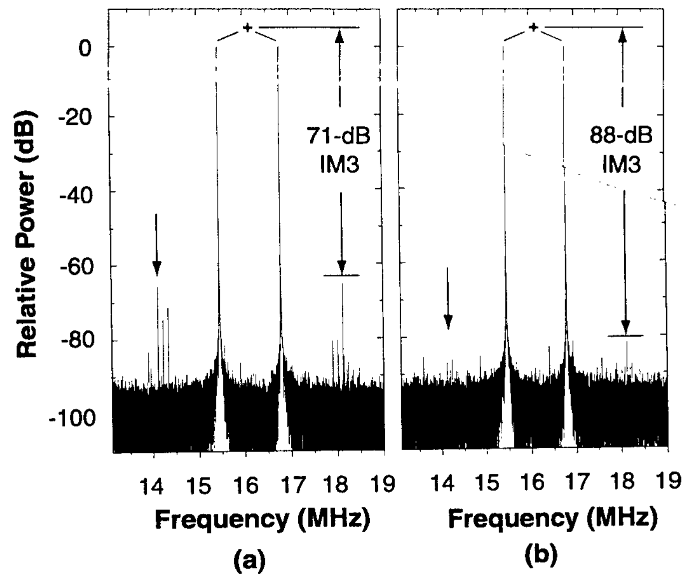

Figure 2-6. Two-tone third-order intermodulation-free dynamic range (IM3) tests of phase-encoded optical sampling system using (a) 50-μm and (b) 300-μm photodiodes.

3. SUBMICROMETER TECHNOLOGY

3.1 ATTENUATING PHASE-SHIFTING MASK AT 157 nm

Attenuating phase-shifting masks (APSMs) are one of the popular resolution enhancing techniques. They have been applied mostly to printing at the contact levels but have also been demonstrated as useful for isolated and dense lines, usually in conjunction with off-axis illumination [1]–[4]. The geometry of an APSM is similar to that of a binary mask, except the absorber layer is replaced with a film (or stack). This film must meet two fundamental requirements: it transmits a small amount of the incident light, ~5–15%, and it retards the phase of this transmitted light by half a wavelength. As a result, negative interference takes place at the edges of open areas, and the slope of the aerial image is sharpened. For the 248-nm exposure wavelength, APSMs are commonly used in manufacturing and the material of choice is MoSi. At 193 nm APSMs are still in the evaluation process. Several material alternatives, such as chrome oxyfluoride [5], MoSiON-based layer [6], Si-based composites [7], and superlattice stacks [8], have been proposed and tested. Much less work has been done to develop 157-nm APSMs. A few candidate materials have been reported [9]–[11], but the limited data indicate that some are modified by laser irradiation during use [12]. Here, we report on the development and lithographic testing of a new APSM for 157 nm. It is simple to prepare and process, it is environmentally stable, and it is robust under laser irradiation. The concept demonstrated here is also easily extendable to 193 nm, and even to 248 nm.

The APSM is a bilayer system, each with independently controlled properties. Such an approach greatly simplifies the search for materials, which would simultaneously meet the requirements of ease of processing, environmental stability, and laser damage stability. The bilayer consists of a thin layer of metal, which is deposited onto the photomask substrate, and which is capped by a transparent thin film. The metal film thickness is determined by the desired transmission of the bilayer. Since it also introduces a phase change in the transmitted wave, the second, transparent film is added at a thickness that would supplement the phase change to a total of π radians.

The metal film chosen in these experiments is platinum, deposited by sputtering under high vacuum conditions, and the transparent film is a cured spin-on-glass (SOG), which chemically is mostly a hydrogen-silsesquioxane (HSQ). The platinum absorber satisfies several key materials requirements: it does not form a native oxide, and therefore it is chemically homogeneous throughout its thickness. Platinum has an extremely fine grain structure. It is also chemically stable, and therefore it can be handled in air, stored for extended periods, and exposed to a variety of solvents without undergoing any changes. The optical properties of this platinum film were determined in the deep-uv and vacuum-uv ranges with a combination of variable-angle spectroscopic ellipsometry and reflectometry. In particular, at 157 nm the real and imaginary parts of its index are $n = 1.444$ and $k = 1.195$, respectively. Figure 3-1 demonstrates how, using these values, one can "dial in" the desired transmission. For instance, in our experiments we have chosen a transmission of 7%, which requires a platinum thickness of 27 nm. Figure 3-1 shows that this thickness also imposes an 80° phase shift, which must be accounted for when the thickness of the SOG

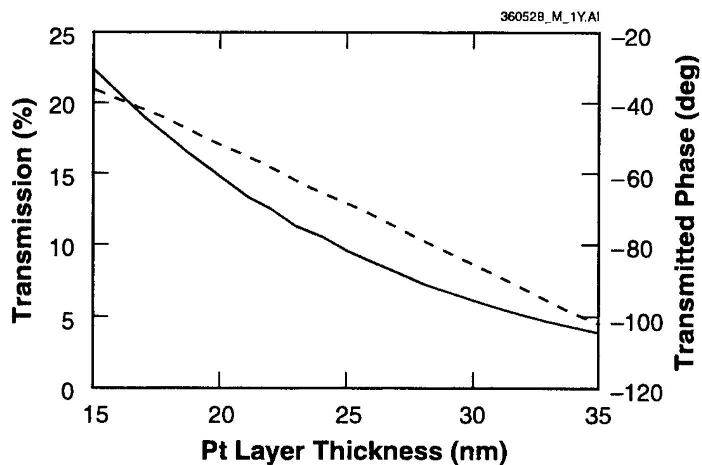

Figure 3-1. Transmission intensity (solid line) and phase (dashed line) of the Pt layer at 157 nm as a function of thickness as predicted from measured optical constants of the film.

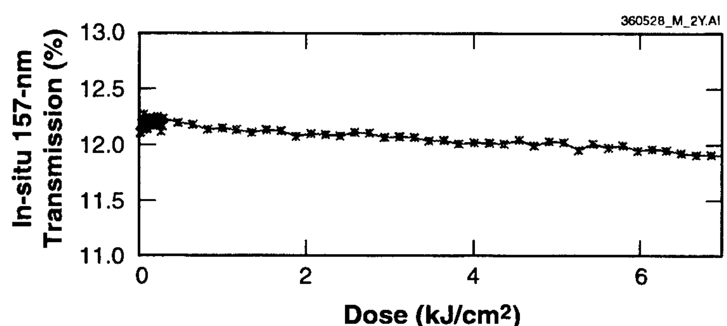

Figure 3-2. In situ 157-nm laser transmission of a Pt/spin-on-glass (SOG) bilayer as a function of incident dose. The incident fluence is 0.15 mJ/cm²/pulse.

layer is calculated. The SOG selected for these experiments is a commercially available HSQ, spin coated onto the platinum film, and cured in air at high temperatures (425°C). Its index of refraction at 157 nm is $n = 1.685$, and $k < 0.001$. When combined with a 27-nm Pt film for use at 157 nm, its thickness is 117 nm.

A critical requirement of APSM materials, often unmet in practice, is stability of optical properties under extended laser irradiation. Many APSMs, both at 193 and 157 nm, have been shown to change their transmission when exposed to laser radiation, even at the low fluences encountered at the photomask. In this respect, the Pt/SOG bilayer stands out for its stability. Figure 3-2 shows that the transmission of the bilayer changes by less than 0.3% over a typical mask utilization lifetime of 6 kJ/cm^2. Separate tests indicated no change in transmission of the Pt layer for doses up to 4 MJ/cm^2. Thus, the small downward trend of the bilayer transmission is probably caused by darkening of the SOG layer.

Figure 3-3 depicts the process flow for preparing a Pt/SOG APSM. The blank substrate is a fluorine-doped fused silica. Following the deposition of Pt and spin coating of HSQ, patterning is carried out with a 50-kV scanning electron beam system and a chemically amplified resist at a thickness of 780 nm. The pattern transfer is obtained in a parallel-plate reactive ion etch system. We have developed a single highly anisotropic etch process that is used for both SOG and Pt:CF_4 etchant gas at 10-mTorr pressure and 250-V self-bias. Under these conditions, the respective etch rates for resist, Pt, and SOG are 25, 3.2, and 14.7 nm/min. With the initial resist thickness of 780 nm, there are still 300 nm of resist left at the end of the etch, and this resist is removed in a conventional photoresist stripper.

The enhanced lithographic performance afforded by APSMs was demonstrated with this bilayer mask on the 0.6-numerical-aperture 157-nm microstepper at International SEMATECH. Although APSMs work best with off-axis illumination, in these initial studies conventional illumination with $\sigma = 0.7$ was used throughout. For comparison, a conventional binary mask was used as well, with the same illumination and the same resist. Figures 3-4(a) and 3-4(b) show scanning electron micrographs of isolated 130-nm spaces and dense 130-nm contacts, respectively, through focus and for three different doses printed using the APSM. These experimental results can be compared to simulations using the ProLith software package. They are summarized in Table 3-1 for isolated spaces and in Table 3-2 for dense contacts. The experimentally observed depth of focus (DOF) of the two masks agrees remarkably well with the simulations. The APSM enables a significantly larger DOF for isolated space features, ~0.5 μm compared to the ~0.35 μm obtained with the binary mask. The exposure latitude results are also qualitatively in agreement with the simulations, the difference being attributed in large part to the relatively coarse grid of doses used in these experiments.

V. Liberman
S. J. Spector
S. C. Cann
M. Rothschild
K. E. Krohn
S. Hien*

*Author not at Lincoln Laboratory.

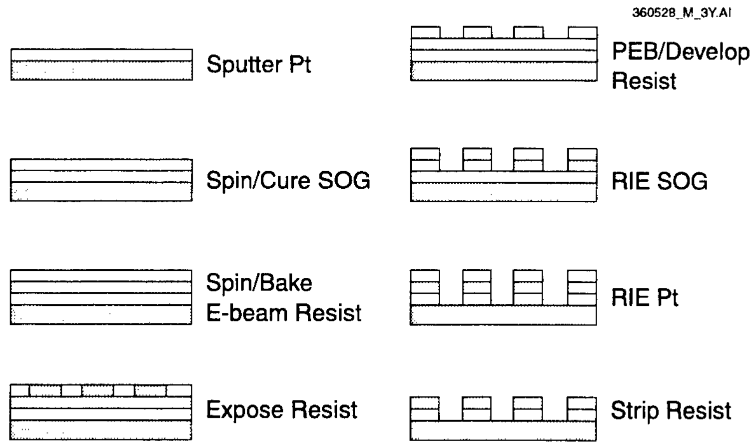

Figure 3-3. Fabrication process flow of the bilayer SOG/Pt stack. PEB = postexposure bake; RIE = reactive ion etch.

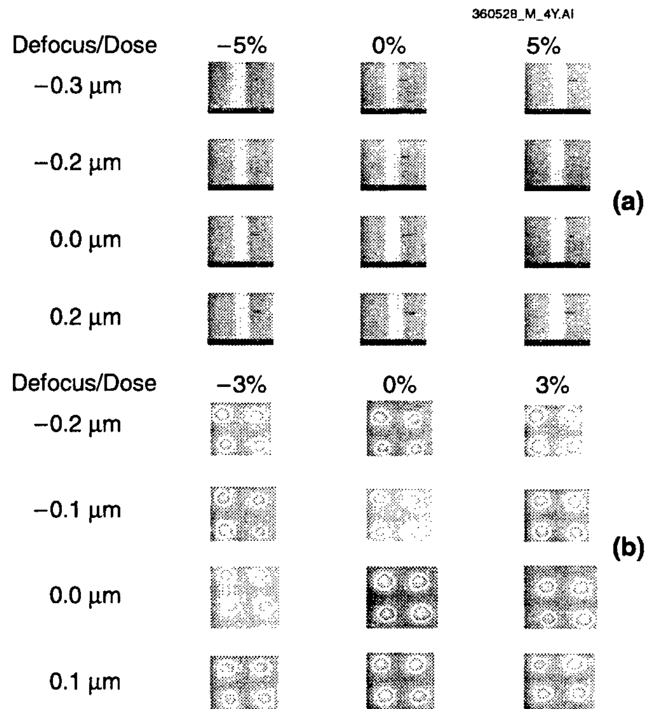

Figure 3-4. (a) Scanning electron micrographs (SEMs) of 130-nm isolated spaces printed with the attenuating phase-shifting mask (APSM), through focus and for three doses; and (b) SEMs of dense 130-nm contact holes printed with the APSM, through focus and for three doses.

TABLE 3-1
Comparison of Lithographic Results with Simulations for 130-nm Isolated Spaces

	APSM		Binary	
	Experiment	**Simulation**	**Experiment**	**Simulation**
Depth of Focus (μm)	0.5	0.45	0.35	0.35
Exposure Latitude (%)	15	13	9	11

TABLE 3-2
Comparison of Lithographic Results with Simulations for 130-nm Dense Contacts

	APSM		Binary	
	Experiment	**Simulation**	**Experiment**	**Simulation**
Depth of Focus (μm)	0.35	0.45* 0.33	0.30*	0.40* 0.29
Exposure Latitude (%)	7.5	11		9

*From Ref. 13. The definition of depth of focus is somewhat different from the ±10% critical dimension control used in this report. Instead, it relies on normalized image log slope.

3.2 LARGE-AREA PATTERNING OF ~50-nm STRUCTURES ON FLEXIBLE SUBSTRATES USING NEAR-FIELD 193-nm RADIATION

New photonic applications, including for example frequency selective surfaces [14], can be facilitated by the ability to pattern deep-submicron arbitrarily shaped structures on flexible substrates. Ideally, such substrates would lend themselves to inexpensive, large-area production, and the patterning must also be high throughput and cost effective for the whole manufacturing process to be of practical interest. Here, we report on one such method, that of using near-field imaging with phase-shifting masks at the 193-nm exposure wavelength. The combination of phase-shifting masks and short-wavelength exposure enables robust sub-100-nm patterning over large areas. Furthermore, the phase-shifting approach ensures that the lithography of the mask has far less stringent dimensions than the features printed on the substrate.

Rigid fused-silica blanks, which can be made transparent to wavelengths as short as 150 nm [15], were used for the phase-shifting contact masks. The conformal, flexible substrates were commercially available sheets of polyimide varying in thickness from ~10 to 100 μm. The resist processing was performed after laminating the sheets via simple contact bonding onto silicon carrier wafers that enabled all processing (spin coat, hot plate bake, develop, thin-film deposition, and etching) to proceed using normal semiconductor manufacturing equipment. The exposures were performed by delamination of the polyimide sheets followed by conformably affixing them to the phase-shifting contact mask. After exposure the sheets were removed from the mask, relaminated onto the silicon carrier wafer, and processed like a normal silicon wafer until the patterning was completed.

Figure 3-5 shows the results of the modeling using the finite difference time domain method [16] of a π-phase step in contact with a photoresist surface. The modeling provided independent outputs for the s- and p-polarized incident radiation, where the p-polarization is normal to the page. Figure 3-5(a) indicates that, for a dose ~2.5× the clearing dose (around a relative intensity of 0.2), unpolarized radiation is expected to yield feature sizes of 45–50 nm (assuming a threshold resist model). The broadening of this linewidth as a function of contact gap is shown in Figure 3-5(b), where, along with Figure 3-5(a), it becomes clear that contact gaps less than ~25 nm and reasonable dose control are needed to realize the minimum feature sizes capable using this technique. These linewidths are consistent with the ~$\lambda/2n$ limit observed for isolated-line widths of ~90 nm produced using 365 nm [17]–[19], where n is the photoresist's refractive index and λ is the exposure wavelength. Correspondingly, we would expect our resolution limit to increase to the ~$\lambda/4n$ limit (~30 nm using 193-nm exposure) experimentally observed for dense features at longer wavelengths [19].

Several 193-nm photoresists were then imaged on silicon substrates using hard contact and the results compared to those generated by the optical modeling. We used silicon substrates to facilitate the initial resist process development as this allowed us to avoid the less routine lamination/delamination processes that used the flexible substrates. Figure 3-6(a) shows the linewidths as a function of exposure dose (normalized for each resist to their respective clearing doses) overlaid with the expected linewidths from Figure 3-5(a) derived by assuming a threshold resist model. The results roughly track with the

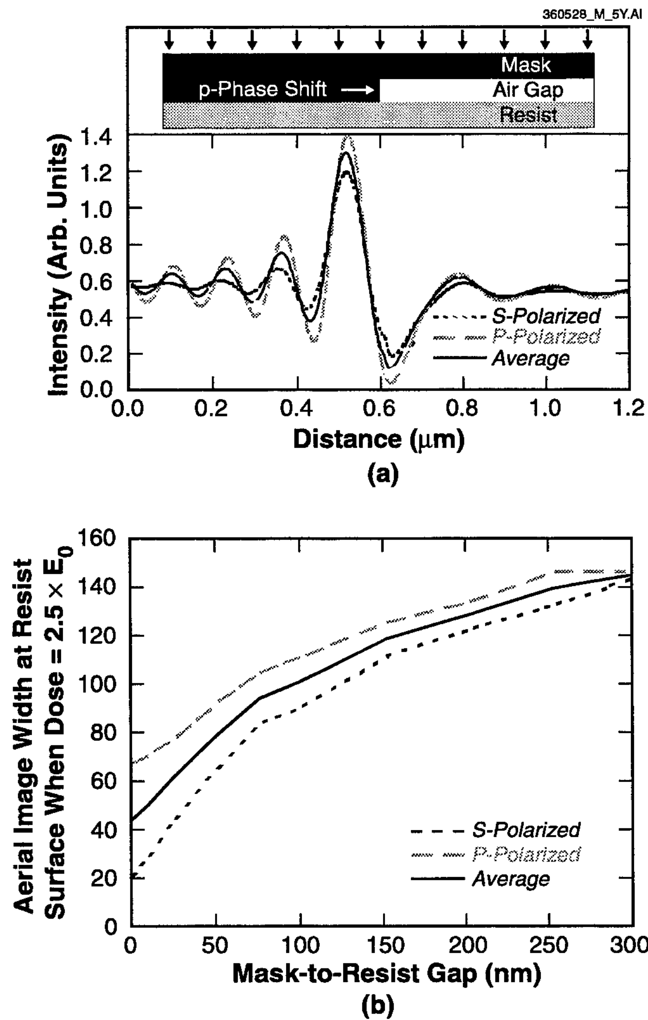

Figure 3-5. (a) Aerial image intensity slices taken at the resist surface when the chromeless phase-shifting mask is in perfect contact with the resist (see insert at top of figure). Shown separately are the intensity slices for s-polarized (parallel to page) and p-polarized (perpendicular to page) light. The exposure wavelength is 193 nm. (b) Image width at intensity = 0.2 as a function of mask-to-wafer gap derived from a compendium of intensity slices taken at the resist surface for simulations as a function of gap. These widths correspond to the expected resist width at an exposure dose ~2.5× the clearing dose, assuming a perfect threshold model of resist development. The actual linewidths will be dictated by resist characteristics. Our experiments used unpolarized light (solid black curve).

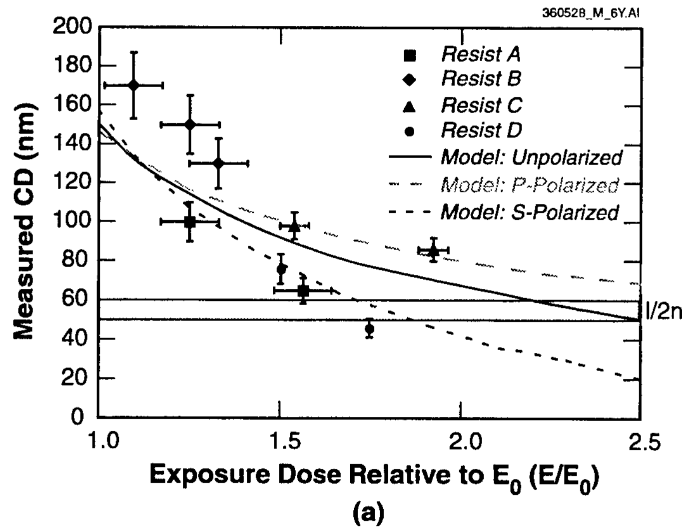

(a)

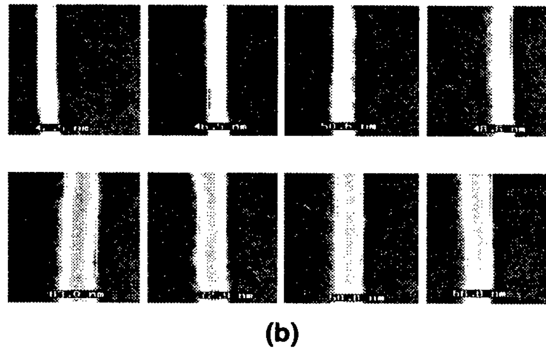

(b)

Figure 3-6. (a) Measured linewidths (symbols) for several commercial 193-nm resists as a function of exposure dose. The exposure doses were normalized to each resist's clearing dose so they could be plotted together. Exposures at doses >2 $\times E_0$ resulted in discontinuous resist lines. Vertical error bars are the range of values obtained over a 1-cm^2 field. Overlaid are the results (smooth curves) from Figure 3-5(a) where the simulated linewidths were tabulated at different intensity values. (b) Top-down electron micrographs of resist D taken at (top) 35-mJ/cm^2 and (bottom) 30-mJ/cm^2 exposure doses, where the average linewidths are 45 and 75 nm, respectively (E_0 = 15 mJ/cm^2). The four images at each dose are taken from different locations across the 1-cm^2 field.

expected linewidths excepting some allowance for the nonidealities of the respective resists. At doses of 2.5× the clearing dose, the lines printed but were discontinuous. We expect this departure of the experimental results from the model to result from resolution limitations in the resists. The best resist, D, was a specially formulated version of a commercially available organosilicon bilayer resist [20], and top-down images of this resist before oxygen-plasma pattern transfer are shown in Figure 3-6(b) for doses of 35 and 30 mJ/cm^2, respectively. Figure 3-7 shows images using the same resist after pattern transfer using different oxygen plasmas. Figures 3-7(a) and 3-7(b) are for image transfer on silicon substrates performed by a high-ion-density helicon plasma, whereas Figure 3-7(c) shows the result for pattern transfer using a reactive ion etcher on a 12.5-μm-thick flexible polyimide film. The residue visible in Figure 3-7(c), which does not appear in Figures 3(a) and 3(b), is a result of the higher bias typical of a reactive ion etch system that causes an increased amount of organosilicon mask sputtering and redeposition, resulting in the observed micromasking [21]. The feature sizes in Figures 3-7(a) through 3-7(c) are all in the range 60–80 nm.

From these experimental and modeling results, it is evident that this approach can produce semi-arbitrary shapes at critical dimensions on the order of 50 nm with ~15% exposure latitude, provided that purely unpolarized light is used. These observations are similar to previous simulations of near-field exposure using the finite-difference time-domain method, which also showed a very strong dependence on polarization [22]. Scaling this process to even shorter wavelengths (e.g., 157 nm) should provide resolution for isolated features on the order of 35–45 nm, with dense features approaching 25 nm and likely limited by mask fabrication and resist performance constraints. The scaling of this approach to large field sizes is limited only by the size of the mask, which currently stands at printable areas of roughly 125 × 125 mm. The prospect of printing ~50-nm features over these large field sizes on flexible substrates, all while using existing resists and thin-film processing equipment, should have application to a variety of engineered photonic surfaces. As with any contact lithography process, there are limitations with regard to defect levels, image placement accuracy, and overlay. Therefore, the process demonstrated here is most suitable to applications with relaxed tolerance in these areas.

R. R. Kunz
M. Rothschild
M. S. Yeung*

*Author not at Lincoln Laboratory.

360528_M_7Y.AI

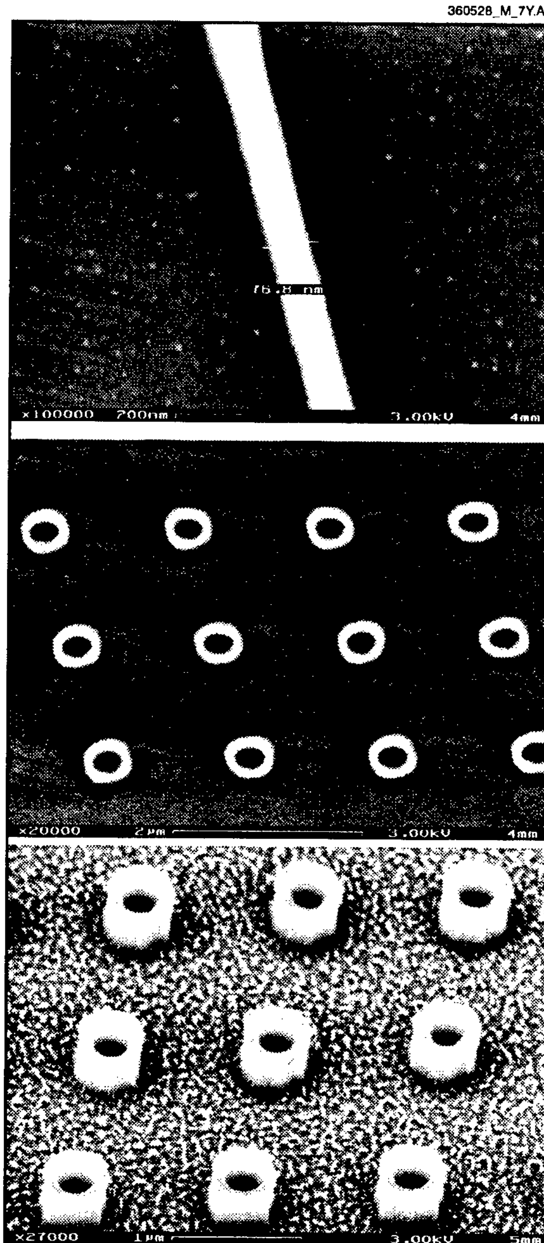

Figure 3-7. (a),(b) Top-down electron micrographs of resist D imaged on silicon following pattern transfer through 200 nm of organic undercoat. The final linewidths are ~75 nm. The pattern transfer was performed using a helicon oxygen plasma (P = 2 mTorr, power = 2500 W, flow = 200 sccm, bias = –50 V). (c) Electron micrograph image of resist D printed on 12.5-μm-thick polyimide after image transfer of the pattern 400 nm into the polyimide layer. The pattern transfer was performed using a reactive ion etcher (P = 15 mTorr, power = 150 W, flow = 200 sccm, bias = –150 V). The aspect ratio is ~5:1.

REFERENCES

1. M. Fritze, P. W. Wyatt, D. K. Astolfi, P. Davis, A. V. Curtis, D. M. Preble, S. G. Cann, S. Deneault, D. Chan, J. C. Shaw, N. T. Sullivan, R. Brandom, and M. E. Mastovich, *Proc. SPIE* **4000**, 1179 (2001).

2. R. J. Socha, W. E. Conley, X. Shi, M. V. Dusa, J. S. Petersen, F. Chen, K. Wampler, T. Laidig, and R. Caldwell, *Proc. SPIE* **3748**, 290 (1999).

3. Y.-M. Ham, S.-M. Kim, S.-J. Kim, S.-M. Bae, Y.-D. Kim, and K.-H. Baik, *Proc. SPIE* **4186**, 275 (2001).

4. C.-M. Wang, S.-J. Lin, C.-H. Lin,Y.-C. Ku, and A. Yen, *Proc. SPIE* **4186**, 359 (2001).

5. K. Nakazawa, T. Matsuo, T. Onodera, H. Morimoto, H. Mohri, C. Hatsuta, and N. Hayashi, *Proc. SPIE* **4066**, 682 (2000).

6. S. Kanai, S. Kawada, A. Isao, T. Sasaki, K. Maetoko, and N. Yoshioka, *Proc. SPIE* **4186**, 846 (2001).

7. S. J. Chey, C. R. Guarnieri, K. Babich, K. R. Pope, D. L. Goldfarb, M. Angelopoulos, K. C. Racette, M. S. Hibbs, M. L. Gibson, and K. R. Kimmel, *Proc. SPIE* **4346**, 798 (2001).

8. P. F. Carcia, R. H. French, G. Reynolds, G. Hughes, C. C. Torardi, M. H. Reilly, M. Lemon, C. R. Miao, D. J. Jones, L. Wilson, and L. Dieu, *Proc. SPIE* **3790**, 23 (1999).

9. B. W. Smith, A. Bourov, L. Zavyalova, and M. Cangemi, *Proc. SPIE* **3676**, 350 (1999).

10. S. Kim, E. Choi, H. Kim, J. Son, and K. No, to be published in *Proc. SPIE* **4691** (2002).

11. T. Onodera, T. Matsuo, T. Itani, and H. Morimoto, *Proc. SPIE* **4346**, 61 (2001).

12. V. Liberman, M. Rothschild, N. N. Efremow, Jr., S. T. Palmacci, J. H. C. Sedlacek, and A. Grenville, *Proc. SPIE* **4691** (2002).

13. H. S. Kim, unpublished material.

14. S. J. Spector, D. K. Astolfi, S. P. Doran, T. M. Lyszczarz, and J. E. Reynolds, *J. Vac. Sci. Technol. B* **19**, 2757 (2001).

15. Y. Ikuta, S. Kikugawa, T. Kawahara, H. Mishiro, N. Shimodaira, and S. Yoshizawa, *Proc. SPIE* **4000**, 1510 (2000).

16. M. S. Yeung, *J. Sci. Comput.* **14**, 121 (1999).

17. J. A. Rogers, K. E. Paul, R. J. Jackman, and G. M. Whitesides, *Appl. Phys. Lett.* **70**, 2658 (1997).

18. J. A. Rogers, K. E. Paul, R. J. Jackman, and G. M. Whitesides, *J. Vac. Sci. Technol. B* **16**, 59 (1998).

19. J. Aizenberg, J. A. Rogers, K. E. Paul, and G. M. Whitesides, *Appl. Opt.* **37**, 2145 (1998).

20. Arch Chemicals, private communication.

21. M. W. Horn, M. A. Hartney, and R. R. Kunz, *Proc. SPIE* **1672**, 448 (1992).

22. S. Tanaka, M. Nakao, M. Umeda, K. Ito, S. Nakamura, and Y. Hatamura, *J. Appl. Phys.* **89**, 3547 (2001).

4. BIOSENSOR AND MOLECULAR TECHNOLOGIES

4.1 CHARACTERIZATION AND DETECTION ALGORITHM DEVELOPMENT OF THE CANARY SENSOR

In order to develop a pathogen sensor that is specific, sensitive, and faster than current methods, we have harnessed the natural detection and signal amplification system of an immune response. B lymphocytes are designed to identify foreign substances within seconds. The cross linking of membrane-bound antibodies by a polyvalent antigen induces a signal transduction cascade, which increases the concentration of cytosolic calcium from internal stores and the environment [1]. We have developed an immortal B-cell line that expresses aequorin, a calcium-sensitive bioluminescent protein found in the jellyfish *Aequorea victoria* [2],[3]. After binding calcium ions, aequorin undergoes a conformational change causing the oxidation of its substrate, coelenterazine, and the emission of light with a peak wavelength of 469 nm [4],[5]. Aequorin-containing B cells [6] are then engineered to be specific by transfection with expression vectors for recombinant antibodies, and emit light when exposed to the biological agent recognized by the antibody. This use of B cells in sensors is called CANARY (Cellular Analysis and Notification of Antigen Risks and Yields).

We have previously demonstrated that we can reliably produce B-cell lines that are specific for a variety of pathogenic agents. We have also developed a centrifuge luminometer format that increases the sensitivity of the B-cell assay by 100-fold, as shown in Figure 4-1, and developed protocols that improve the reliability and performance of the cells from day to day. Here, we provide results of a blind test administered by Dugway Proving Grounds, show the development and testing of a detection algorithm that optimizes the false-alarm rate, and demonstrate reliability of the CANARY sensor over time.

Blind trials conducted at MIT Lincoln Laboratory (JFT-6 take-home trial) tested the speed, sensitivity, and false-alarm rate of the CANARY biosensor by analyzing 256 samples that contained *Francisella tularensis* and two other agents for which we did not have specific B-cell lines. Owing to the speed of the assay (>3 min per test), we were able to complete two day's worth of assays each day (approximately 100 tests) and in most instances were done by noon. These trials enabled us to identify one type of medium, phosphate buffered saline, as a source of false positives and demonstrate that the false-positive rate is lower for samples in CO_2-Independent (CO_2I) medium, as shown in Table 4-1. In addition, our analysis of the results led to a refined detection algorithm that reduces the false-positive rate without greatly affecting the sensitivity. The initial detection algorithm, illustrated by the purple box in Figure 4-2, defined a positive result as a signal that exceeded 3 times the background level 10–50 s after the B cells were centrifuged on top of the concentrated agent. However, over 90% of the false positives were observed to peak after 30 s. By reducing the window of the detection algorithm to 15–30 s, and including the requirement that the signal reach a peak within that window, we were able to significantly reduce the false-positive rate, as seen in Table 4-1. We performed additional experiments, both blind and open, to test the refined algorithm. In these experiments we were able to demonstrate a rate of false positives of 0.3%

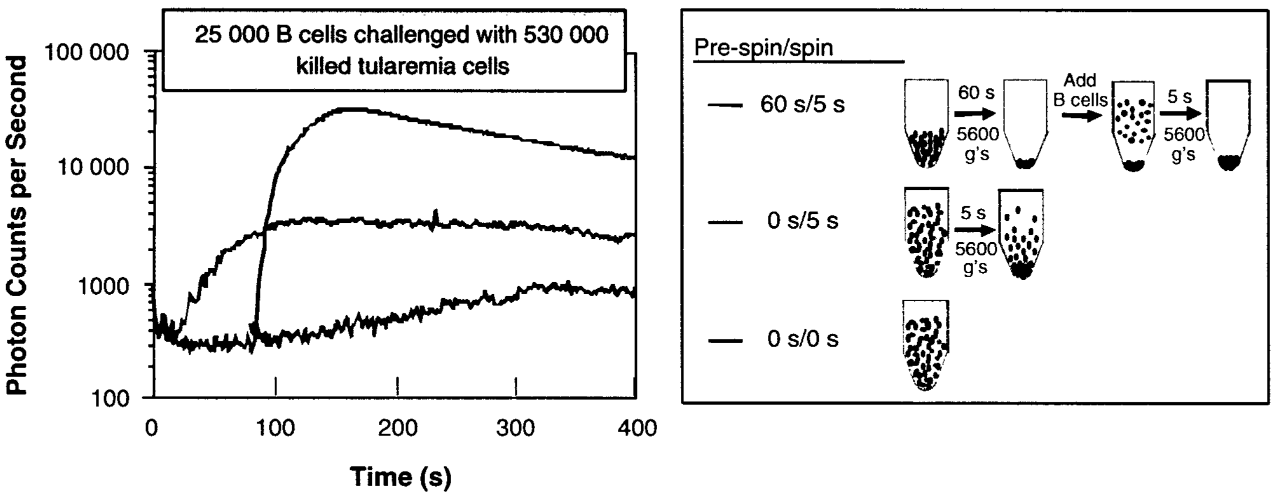

Figure 4-1. Centrifugation format providing increased sensitivity and speed. Top: Photographs of centrifugation setup in (left) spinning (13,000 rpm) and (right) resting/measuring modes. Bottom: Plot of photon output produced by exposure of 25,000 B cells to 530,000 killed tularemia particles with and without centrifugation enhancement procedures as indicated in the schematic at right, where tularemia particles are represented by black circles and B cells by larger red circles.

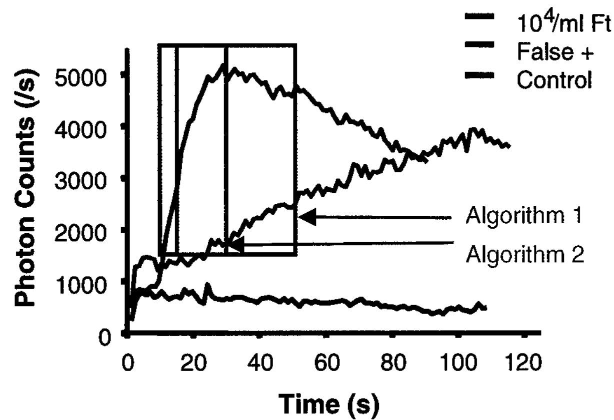

Figure 4-2. Algorithm development.

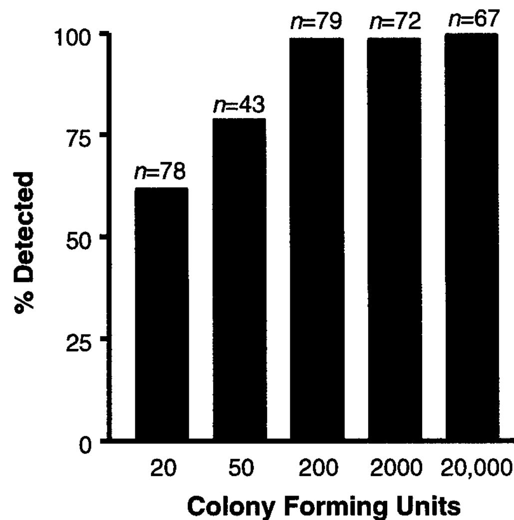

Figure 4-3. Sensitivity of B-cell line specific for Yersinia pestis.

while maintaining an 87% probability of identification against 10^4 colony-forming units (cfu) per milliliter of *F. tularensis*, as shown in Table 4-2.

The results of an extensive analysis of the B-cell line specific for *Yersinia pestis*, the bacterium that causes the plague, are shown in Figure 4-3. Tests performed both blind and open over a period of several months were analyzed using the refined algorithm developed from the JFT-6 take-home trial. We can demonstrate detection of 20 and 50 cfu for 62 and 79% of the time, respectively, and detection of 99% or better at 200 cfu. Furthermore, the false-positive rate using CO_2I remains <0.5%.

TABLE 4-1
CANARY False-Positive Rate

Sample Medium	Algorithm 1	Algorithm 2
PBS/FBS*	83/1040 = 8%	27/1040 = 2.6%
CO_2I	32/883 = 3.6%	3/883 = 0.3%
*Phosphate buffered saline containing 5% fetal bovine serum.		

TABLE 4-2
CANARY Sensitivity for *Francisella tularensis*

F. tularensis Concentration	Algorithm 1	Algorithm 2
10^3/ml	28/60 = 47%	22/60 = 37%
10^4/ml	61/67 = 91%	58/67 = 87%
10^5/ml	65/65 = 100%	65/65 = 100%

In summary, we have performed extensive characterization and refined the detection algorithm to demonstrate the reliability and sensitivity of the CANARY sensor. In fact, for every pathogen we have tested that is large enough to be concentrated in a microcentrifuge ($n = 6$), we have observed similar levels of sensitivity, approximately 50 cfu or 50 plaque-forming units (data not shown). The false-positive rate of 0.4% ($n = 1288$), combined with a level of sensitivity approaching that of the polymerase chain reaction technique and an assay time of a few minutes, makes CANARY one of the most promising pathogen identification technologies currently in development.

M. S. Petrovick

REFERENCES

1. H. A. Wilson, D. Greenblatt, M. Poenie, F. D. Finkelman, and R. Y. Tsien, *J. Exp. Med.* **166**, 601 (1987).

2. M. J. Cormier, D. C. Prasher, M. Longiaru, and R. O. McCann, *Photochem. Photobiol.* **49**, 509 (1989).

3. O. Shimomura, B. Musicki, and Y. Kishi, *Biochem. J.* **261**, 913 (1989).

4. F. I. Tsuji, S. Inouye, T. Goto, and Y. Sakaki, *Proc. Natl. Acad. Sci. USA* **83**, 8107 (1986).

5. O. Shimomura and F. H. Johnson, *Proc. Natl. Acad. Sci. USA* **75**, 2611 (1978).

6. D. Button and M. Brownstein, *Cell Calcium* **14**, 663 (1993).

5. ADVANCED IMAGING TECHNOLOGY

5.1 RESPONSE OF MOLECULAR BEAM EPITAXY–PASSIVATED BACK-ILLUMINATED CHARGE-COUPLED DEVICES TO LOW-ENERGY X RAYS

For a charge-coupled device (CCD) to have good sensitivity to a wide range of x-ray energies, it is necessary to perform special wafer processing. Obtaining a good response to low-energy x rays requires a back-illuminated (BI) CCD imager [1] because the photons may be absorbed in the polysilicon gate structure on the front of the device; in this instance photoelectrons are not created where they may be collected and read out by the CCD. On the other hand, higher-energy x rays have longer absorption lengths that, in turn, require thick BI detectors. In order to fabricate such a device, it is necessary to produce a conventional CCD, thin it from the back side to ~40 μm, and passivate this back surface. The thickness is chosen as a compromise between the requirement to fully deplete the device for minimal lateral diffusion of the event cloud and the desire for maximum absorption of x rays for $E > 5$ keV. The passivation decreases the fraction of photoelectrons that recombine on the back surface and also provides an electric field that drives the electrons towards the depleted region of the device. In the past, we have fabricated CCD x-ray detectors using what we have referred to as the refractory process (REF), where the back-side passivation was produced by oxidizing the back side, ion implanting it with boron, and annealing in a conventional semiconductor processing furnace; this process produces a p^+ region on the back of the device [2].

We have recently developed a process to fabricate the p^+ region by molecular beam epitaxy (MBE) on the thinned CCD wafer [3]. Briefly, the wafers are thinned to 45 μm, cleaned, and then outgassed by heating to approximately 430°C in an ultrahigh vacuum chamber. The clean Si surface reconstructs during heating, changing from an initial 1×1 to a 2×2 reflection high-energy diffraction pattern. About 5 nm of p^+ Si is grown on the wafer back side, with a B concentration around 1×10^{20}/cm^3. This back-side passivation process is similar to one developed at the Jet Propulsion Laboratory [4]. After MBE growth, the devices are processed to contact the metal bond pads, packaged, and tested.

The MBE and REF devices both collect 90–95% of the theoretical number of photoelectrons at 525 eV, compared to only 30–40% for the front-illuminated (FI) device, leading to a significant advantage in imaging faint x-ray sources. We believe the MBE process should also have a quantum efficiency of ~70% at C Ka peak at 277 eV, as measured on the REF parts [2]; the FI parts had a quantum efficiency of <1% at this energy. It should also be mentioned that the MBE devices have a higher processing yield than do REF parts, having fewer hot pixels and hot columns.

Since the O Ka x ray at 525 eV has an absorption depth of ~530 nm, imaging its photons is a sensitive test of the CCD's ability to collect soft x rays and to determine their energy. This energy is quantified by counting the number of electrons in a pixel and assuming that one electron is generated for every 3.65 eV in the absorbed photon. Some photoelectrons may, however, diffuse laterally into another

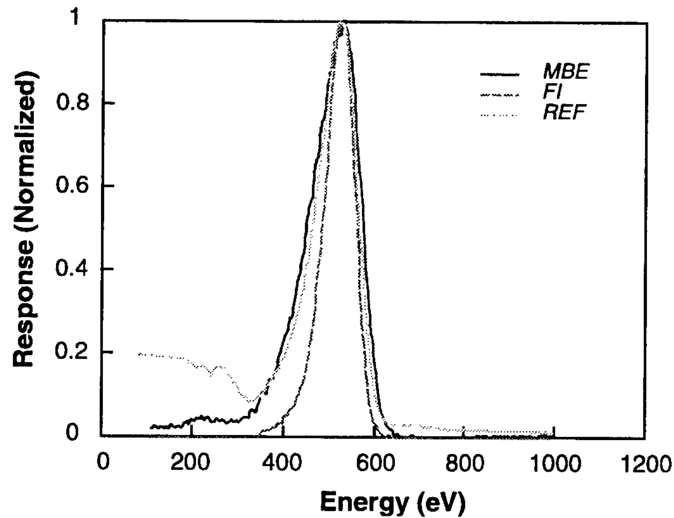

Figure 5-1. Oxygen x-ray response.

pixel before they are collected in the buried channel of the CCD, leading to fewer electrons in a given pixel than the theoretical value.

The results of exposing several BI CCDs to an O Ka source are shown in Figure 5-1, where the abscissa is the energy corresponding to the number of electrons and the ordinate is the count of events containing this number of electrons, normalized to the peak value. In all cases, the peak occurs at 525 eV, within experimental accuracy. It was not possible to obtain results for CCDs with the same architecture under all back-side processing conditions, so there are differences in the pixel size and pixel layout among the devices, but the initial front-side processing conditions of the wafers were nominally identical. The narrowest peak was obtained using an FI imager, of the type referred to as a CCID34, which has a 10-μm-square pixel in a 6144 × 3072 array. The next narrowest peak is a CCID17 device, the kind used for the Chandra X-Ray Observatory; this has 24-μm pixels in a 1024 × 1024 array. This BI device had been processed using the older ion-implant and anneal process. The last curve is for a CCID20 that has a 15-μm pixel in a 4096 × 2048 array; note this device has the same physical footprint as a CCID34. The CCID20 is also a BI detector, where the p^+ layer had been grown by MBE. We note in passing the rise in response of the REF part for energies <300 eV; this is probably due to contamination of the oxygen plasma that generated the x rays.

The full-width at half-maximum (FWHM) for each of the devices plotted in Figure 5-1 is shown in Table 5-1, as well as a range for the FWHM. The FI device has the narrowest peak, which is not surprising since it has a slightly higher charge transfer efficiency (≥0.999998) than do the BI devices (≥0.99998). Comparing the BI devices, the REF device has a narrower peak in this instance, which would allow for

TABLE 5-1
Oxygen X-Ray Peak Widths

CCD Processing	Device Architecture	Displayed FWHM (eV)	Range of FWHM (eV)
Front-Illuminated	CCID34	77	70–90
Back-Illuminated Refractory Process	CCID17	103	100–200
Back-Illuminated Molecular Beam Epitaxy	CCID20	125	120–145

better resolution of an x-ray spectrum. For the limited number of samples tested so far, however, the MBE device is much more consistent in the range of peak widths measured. The consistency of the peak widths for the MBE process is a valuable attribute when assembling, calibrating, and using focal plane arrays of CCDs.

The reason for the variation in peak widths is not well understood at the present, but it does not appear to be related to differences in pixel size, to first order. Nor is it caused by incomplete depletion of the 45-μm thickness, as the peak widths remain the same while varying clock biases during testing. Further optimization of the MBE process is expected to lead to stronger electric fields on the back side and to narrower peak widths.

Although the BI parts have somewhat degraded resolution compared to the FI device, it is important to recall their absolute quantum efficiency is much higher (note that Figure 5-1 plots a normalized response). These differences in performance and processing yield suggest the MBE process is preferred over FI or REF CCDs for large focal planes where high sensitivity and moderate resolution are needed to detect low-energy x rays.

J. A. Gregory B. E. Burke
S. D. Calawa P. M. Nitishin
A. H. Loomis S. E. Kissel*
G. R. Ricker* M. W. Bautz*

* Author not at Lincoln Laboratory.

REFERENCES

1. B. E. Burke, J. A. Gregory, A. H. Loomis, C. C. Cook, D. J. Young, M. J. Cooper, T. A. Lind, G. A. Luppino, and J. L. Tonry, *Optical Detectors for Astronomy II*, P. Amico and J. W. Beletic, eds. (Kluwer, Norwell, Mass., 2000), p. 187.

2. J. A. Gregory, A. H. Loomis, B. E. Burke, and G. Y. Prigozhin, Solid State Research Report, Lincoln Laboratory, MIT, 1994:4, p. 31.

3. S. D. Calawa, B. E. Burke, P. M. Nitishin, A. H. Loomis, J. A. Gregory, and T. A. Lind, to be published in *J. Vac. Sci. Technol. B*, May-June 2002.

4. M. E. Hoenk, P. J. Gruthaner, F. J. Grunthaner, R. W. Terhune, M. Fattahi, and H.-F. Tseng, *Appl. Phys. Lett.* **61**, 1084 (1992).

6. ANALOG DEVICE TECHNOLOGY

6.1 ANALOG ARRAY PROCESSOR FOR CANCELLATION OF UNDESIRED SIGNALS IN RF FRONT ENDS

In many rf systems the dynamic range can be limited by large signals of either hostile or friendly origin that overload either the rf low-noise amplifier or the analog-to-digital converter. Since this overload occurs at the front end, it cannot be removed by digital signal processing techniques. Adding limiters or attenuators is one approach to remove the overload, but since they add rf loss, the receiver sensitivity is decreased. A more effective approach is to remove the undesired signal without adding loss to the desired signal. Techniques in this category include tunable notch filtering and signal subtraction. Tunable notch filters have the limitation that all signals in and near the band stop region are attenuated. Thus, this technique is ineffective for situations where the desired and undesired signals are closely spaced, such as signal intelligence (SIGINT) interception of low level communication signals "hiding" under a strong transmitter, or electronic warfare scenarios where one desires to simultaneously jam and intercept an adversary communication signal. Another technique for signal cancellation is simply to subtract the undesired signal from the rf front end. This is possible in situations where the undesired signal is known, such as in cosite interference rejection. However, there are situations where interference rejection is difficult even when the undesired signal is known, such as heavily multipathed environments in urban areas and on board naval surface ships. A new cancellation technique has been developed to address these difficult situations. Such a system must be low loss to preserve the noise figure, and it should be passive to prevent overload and spurious signal generation. The requirements for low loss and passivity naturally suggest that superconducting technology could be used advantageously in this application.

In the new cancellation technique, the undesired signal is diverted to a terminated port in the analog signal domain. This is accomplished by phase shifters and a new device termed the power diverter (PD). The details of the PD circuit will be discussed in a later publication. It is composed of a novel arrangement of 90° hybrids and phase shifters, allowing it to be realized with standard microwave components. Functionally, the PD performs an externally programmable rotation on the two inputs, as is shown in Figure 6-1. Internally it uses voltage-controlled phase shifters to accomplish the function. Mathematically, if the inputs are A_1 and A_2, then the outputs B_1 and B_2 are

$$\begin{aligned} B_1 &= \left(A_1 \cos\theta + A_2 \sin\theta\right) \\ B_2 &= \left(-A_1 \sin\theta + A_2 \cos\theta\right) \end{aligned} \tag{6.1}$$

This is equivalent to a rotation of the vector

$$A = \begin{pmatrix} A_1 \\ A_2 \end{pmatrix} \tag{6.2}$$

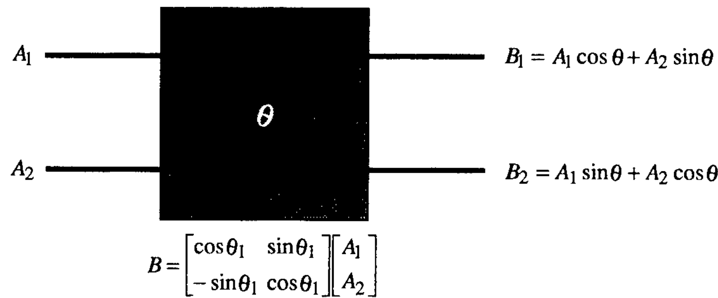

Figure 6-1. Power diverter. Inputs are A_1 and A_2. The angle θ is externally programmable.

by the angle θ. It also preserves the total power, and thus is lossless. For the PD to function, the signals must be in phase, which is accomplished by the phase shifters at the inputs.

An illustration of an rf front end with the cancellation system is shown in Figure 6-2. Pictured are three antennas that each feed an input port of the cancellation circuitry. Ideally, the cancellation operation is unitary and lossless, so the energy from the undesired signal is dumped to one of the output ports. The signals to the other two output ports are a linear combination of the three input ports, and the transformation from the input to the output is known. If the system is extended to a larger number of input ports, the energy from the undesired signal can still be directed to a single output port, and the desired signal will be output on the remaining ports. As the cancellation technique is extended to a larger number of input ports, the signal cancellation is handled on a port-by-port (serial-like) basis. The advantage of this approach is that there are no requirements on the phase relation of the undesired signal as it appears in the successive ports. Thus, this cancellation technique is fundamentally different from applying beamforming weights on the input ports to form a high gain beam on the desired signal and a null on the undesired signal.

Figure 6-2 shows in detail the mathematics of choosing the coefficients of the power diverter so that all of the power appears in one of the outputs, which would be appropriate for a system where the desired signal could be turned off while the system adapts to reduce the interference. In this case the other two channels would be available for reception of the desired signal with more than 30-dB reduction of the interference.

We have built a laboratory demonstration of the single-frequency analog signal processing subsystem using conventional, connectorized, off-the-shelf components. We have implemented a three-channel example of a narrow bandwidth system, illustrated in Figure 6-2. A photograph of the breadboard system is shown in Figure 6-3. The approximate volume of the analog circuitry is $6 \times 12 \times 1$ in. Interference suppression of up to 40 dB has been demonstrated.

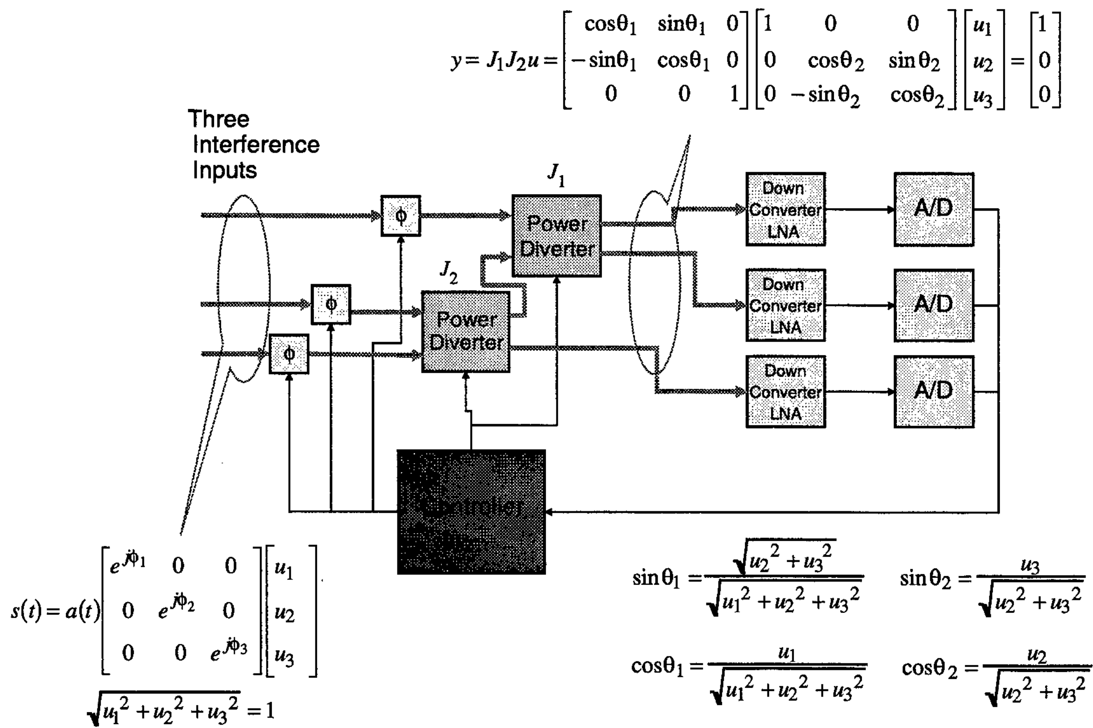

Figure 6-2. Hardware demonstration of interference cancellation. s(t) is the input with arbitrary normalized amplitude and phase, simulating the interference signal. The power diverters are programmed to perform rotations θ_1 and θ_2 as given by the equations at the lower right. The result is that in the output signals y the interference appears on one output channel only, and the other two channels are interference free and can be used to receive a desired signal that can be added to the input.

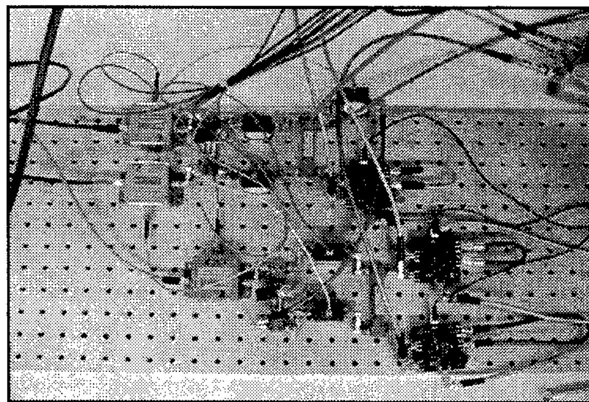

Figure 6-3. Photograph of the analog processing part of the bench-top demonstration.

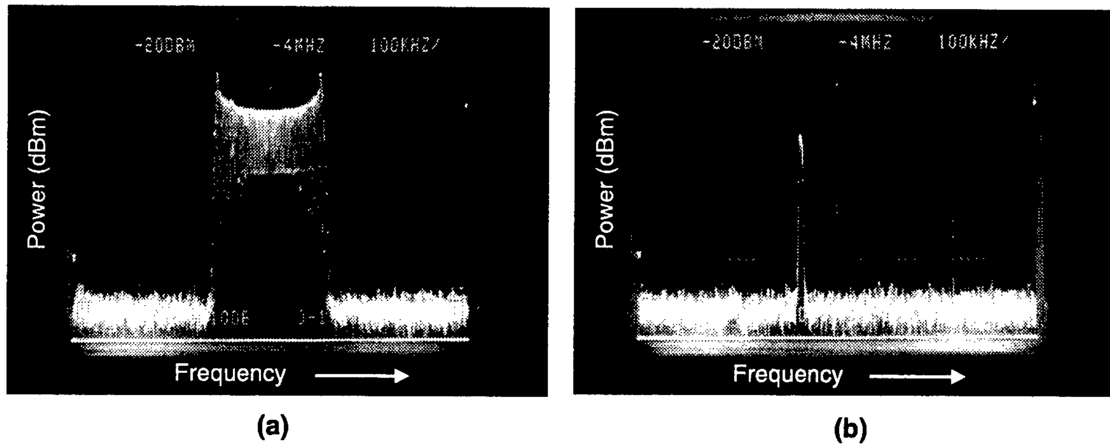

Figure 6-4. (a) Spectrum analyzer trace without any signal cancellation. Both a desired cw signal and a frequency modulated interferer are present. The interferer is completely masking the desired signal. (b) Output after the interference cancellation is turned on.

We have built the basic system and demonstrated that the indicated signal cancellation can be achieved. The frequency of operation was chosen to be 850 MHz. We have demonstrated the cancellation of a large interfering signal in the presence of a smaller desired signal simulated to be arriving at a different angle from the interferer but at the same frequency. Figure 6-4 shows the measured results obtained with the breadboard system. The photograph at the left shows the output trace of a spectrum analyzer connected to one of the three channels of the breadboard without signal cancellation and with the presence of a frequency modulated interference that is masking a cw desired signal. With the interference cancellation turned off, the input of each channel is passed directly to the output. The interferer masks the desired signal completely. The picture on the right shows the output of the channels after the cancellation is turned on. The interference is reduced by more than 50 dB in this case, and the desired signal can be clearly observed.

D. E. Oates

7. ADVANCED SILICON TECHNOLOGY

7.1 MICROELECTROMECHANICAL SYSTEMS RELIABILITY STUDY

The packaging and reliability of rf microelectromechanical systems (MEMS) devices are the crucial factors in the success or failure of MEMS devices for rf and microwave circuit applications. Some applications, such as antenna diversity switches and switched filter banks for portable and satellite communications, require less than 1 billion switch cycles over the lifetime of a product. However, many radar and instrumentation applications require 10–200 billion switch cycles. Proving reliability above 100 billion cycles in a packaged MEMS switch is the major milestone for rf MEMS manufacturers looking to supply parts for defense radar systems.

The accomplishment of 100 billion or more cycles is still not enough for many applications. Extended hold down times (1 min to several months) may be required for some switch applications. This is actually a challenge to rf MEMS switches where time to failure of many devices is often less than a few minutes when held in the down state. The goal of our effort is to assess and improve the switch cycles reliability and the hold down reliability of the rf MEMS devices developed at MIT Lincoln Laboratory. In the course of our effort, we have demonstrated >10 billion switch cycles for a MEMS capacitive switch and hold down times greater than 24 h.

A scanning electron micrograph (SEM) of the capacitive series switch in its released state is shown in Figure 7-1. These switches were fabricated in the MIT Lincoln Laboratory Microelectronics Laboratory using CMOS compatible surface micromachining techniques. The switch membrane is composed of three layers: 100-nm SiO_2, 300-nm Al, and 100-nm SiO_2. The switch is curled up in the released state by the control of the residual stress in the top and bottom silicon dioxide layers. The switch is actuated by applying an electrostatic force between the switch membrane and a pull down electrode buried beneath the switch. The device has an up state capacitance of 8–10 fF and a down state capacitance of 1–1.4 pF, making it suitable for applications from X-band to K-band.

The cycles testing of our rf MEMS capacitive devices was performed in a clean testing environment under flowing nitrogen. The circuit shown in Figure 7-2 was used to supply the bias voltage to the devices as well as measure the up and down state capacitances. The bipolar bias voltage waveform was generated using an arbitrary waveform generator and a high voltage amplifier. A 10-MHz sine wave is applied to the input of the switch and the coupled signal is used to measure the switch capacitance. The setup is controlled by a personal computer that records the capacitance in the up and down state at various intervals during the test.

The waveform was designed to have a nearly 50% duty cycle and has a repetition rate of 2.5 kHz. The waveform has a high voltage kick V_k of 40 V lasting 20 μs and a hold voltage V_h of 20 V lasting 130 μs. These values were optimized experimentally to be as low as possible while still allowing for switch actuation. Previous tests with higher voltages resulted in reduced switch lifetimes.

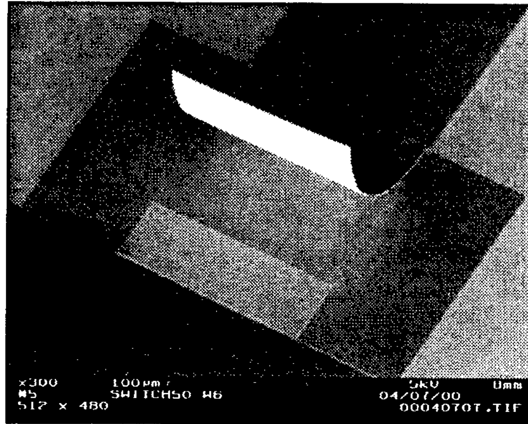

Figure 7-1. Scanning electron micrograph (SEM) of the MIT Lincoln Laboratory rf microelectromechanical systems (MEMS) capacitive switch.

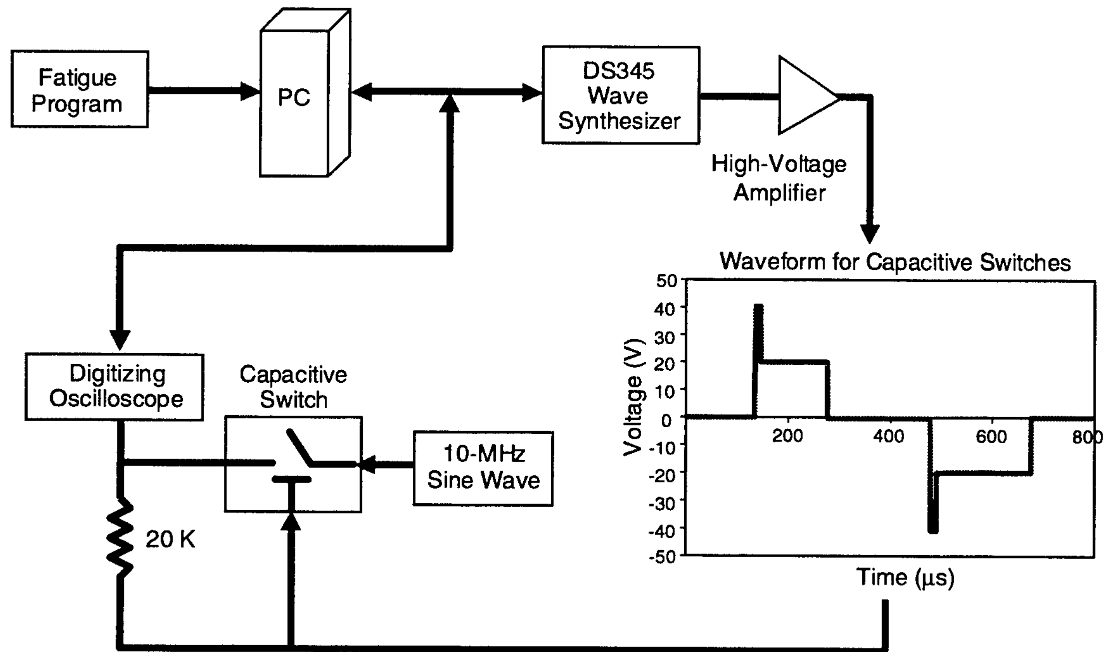

Figure 7-2. Illustration of switch cycle test setup. A bipolar waveform was used to actuate the devices.

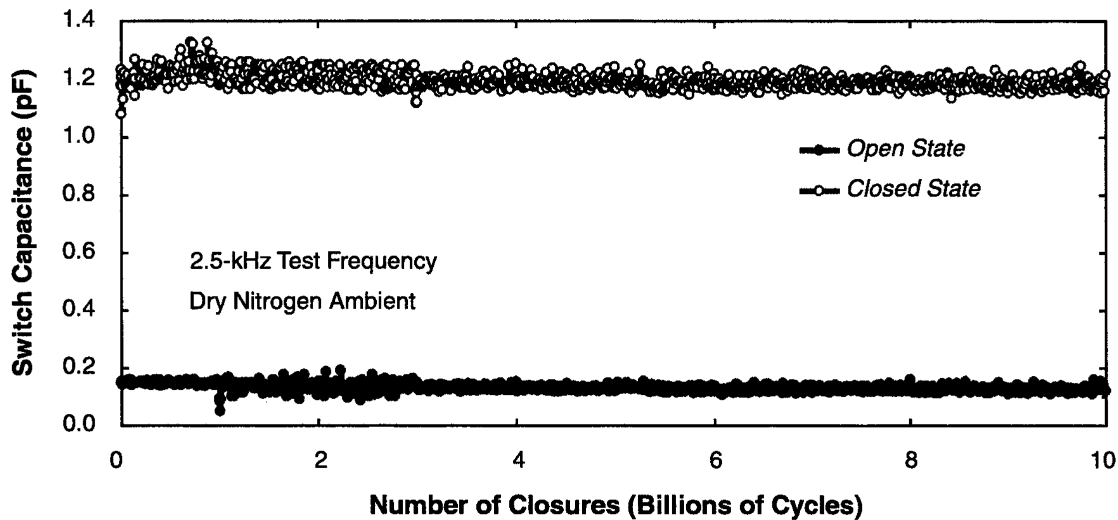

Figure 7-3. Measured switch capacitance in the up and down state after various numbers of switch cycles.

The switch was tested to 10 billion cycles. The data showing the capacitance in the up and down state after various numbers of switch cycles are shown in Figure 7-3. After successful completion of 10 billion cycles, the switch was measured on an rf probe station to characterize its performance. The rf performance and the extracted capacitance value were within 5% of the pretest values.

Similar devices were tested until failure in hold down experiments. The tests were performed by slowly increasing the amplitude of a 100-Hz bipolar bias voltage until the switch was actuated to the down state. The voltage at which this occurred was recorded as the pull down voltage (35–40 V for most devices). The voltage was reduced to the hold voltage V_h for a period of time. The voltage was then slowly reduced until the switch released from the substrate, and the voltage at which it released was recorded as the release voltage V_r.

A typical hold down history is shown in Figure 7-4. The bias waveform is a 100-Hz bipolar square waveform. The hold voltage was set to 15 V for this particular switch. The results are typical of most devices in that the release voltage decreases with subsequent hold down cycles, indicating some type of charging effect. At some point in the test, the switch will not release from the substrate. This is recorded as the time to failure. At that point the switch will release after a period of no bias voltage and that time is recorded. The time to release after failure also increases with subsequent hold down cycles. Periods of inactivity, as well as high-temperature treatments, seem to help the switch recover. Blaise and Sarjeant [1] have shown that heat treatments and uv light exposure cause trapped charges in dielectrics to "detrap" or discharge. This is consistent with our experience.

Because a charging mechanism is suspected in the failure of the MEMS capacitive switches, the failure should be a function of the applied electric field in the dielectric layers in accordance with

Frankel-Poole and Fowler-Nordheim phenomena. An additional experiment was performed where total time to failure was recorded for different hold voltages. The results are shown in Figure 7-5 and demonstrate an exponential relationship between the time to failure and the applied hold voltage. A better understanding of the charging mechanisms are required to develop a theoretical relationship between the time to failure and the applied hold voltage under bipolar conditions.

Another, more abrupt failure mechanism occurs at localized positions within the contact region of the capacitive switches. In these cases, the switch will appear to be tacked at a small point and will not release, as shown in Figure 7-6. SEM inspection of the tack point after forcible release shows a corresponding puck and divot pair at the local tack point, indicating a surface bond strong enough to pull a small amount of SiO_2 from the bottom layer and attach it to the top layer. This type of bond between oxide materials is often caused by a chemical reaction involving absorbed moisture and hydroxylated surfaces.

Switch cycle reliability of more than 10 billion cycles was achieved for the MIT Lincoln Laboratory capacitive rf MEMS series switch. Testing continues in an effort to extend this number to the 10's of billions. Hold down times for our devices are a strong function of the applied voltage, suggesting dielectric charging as a mechanism for failure. While the hold down times of our current switches are longer than other reported times for similar switches, practical applications in many systems require even longer hold down times. Results from tests on the MIT Lincoln Laboratory microshutters have yielded hold down times of greater than three months. Continued testing and design improvements should yield improved switch cycle and hold down reliability as well as improve our understanding of the failure mechanisms.

J. Muldavin C. Bozler
A. Soares E. Austin
J. Howard L. Travis
S. Rabe

REFERENCE

1. G. Blaise and W. J. Sarjeant, *IEEE Trans. Dielectr. Electr. Insul.* **5**, 779 (1998).

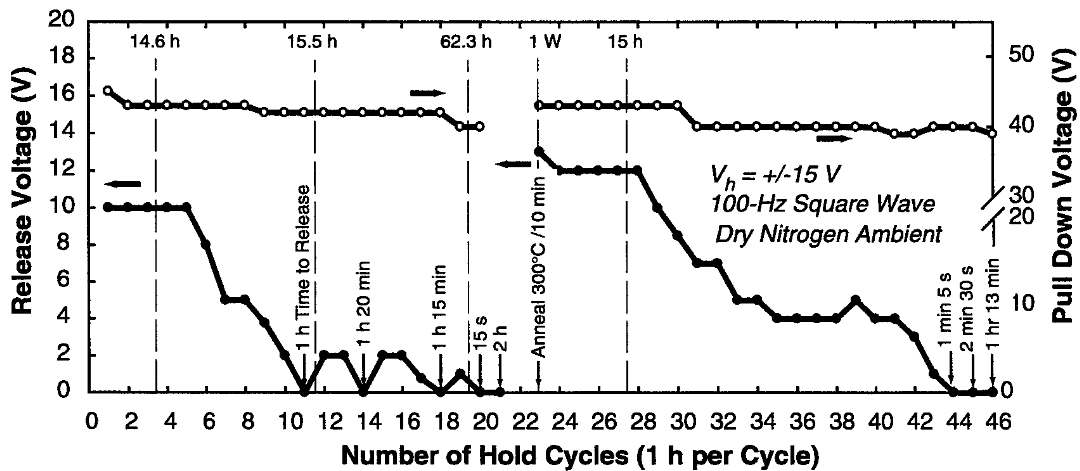

Figure 7-4. Hold down history for a MEMS capacitive switch showing dielectric charging and discharge. Values for times to release after failure are shown. The vertical dashed lines indicate pauses in the experiment with pause times as indicated.

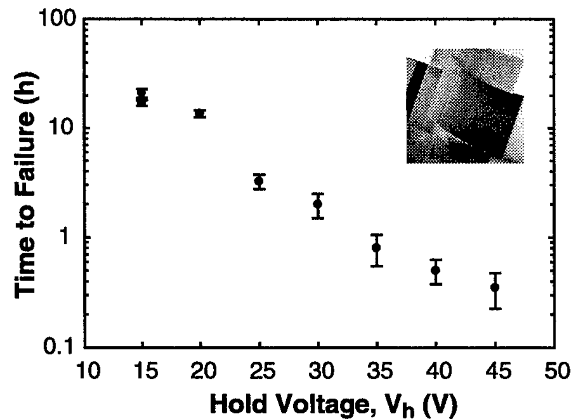

Figure 7-5. Time to failure vs hold voltage for identical MEMS capacitive switches.

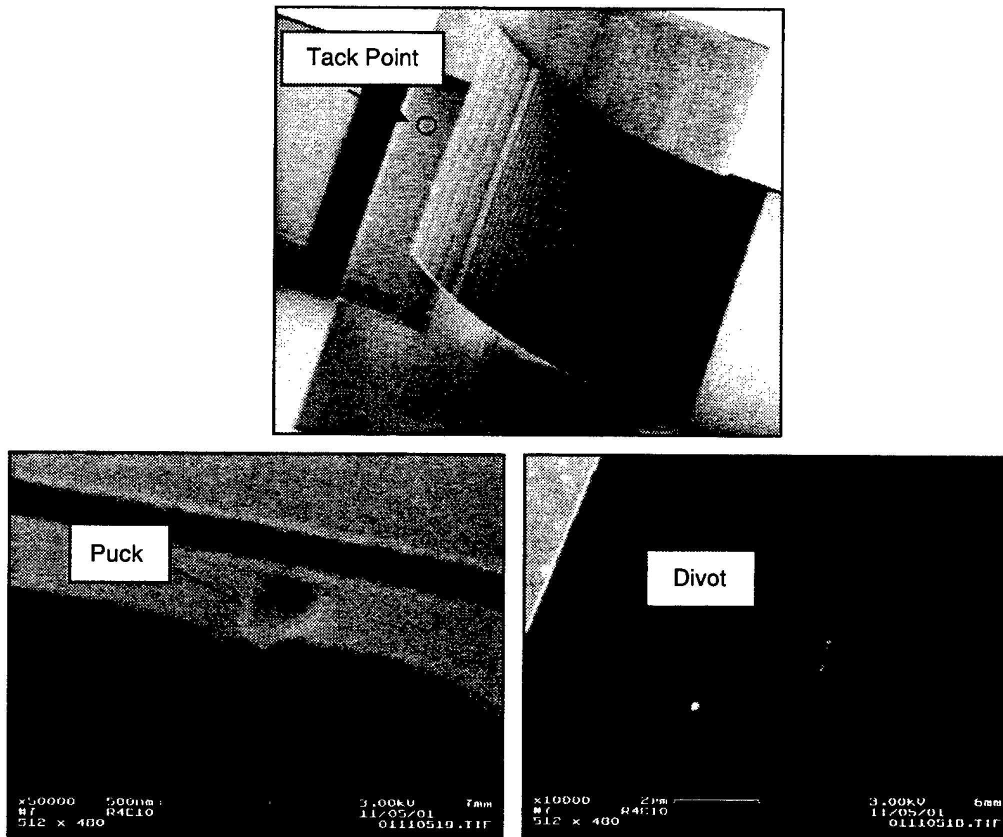

Figure 7-6. SEMS showing a tack point on a rf MEMS capacitive series switch. Close-up SEMs show a puck and divot at the tack point, indicating a strong surface bond at that point.

REPORT DOCUMENTATION PAGE

Form Approved
OMB No. 0704-0188

Public reporting burden for this collection of information is estimated to average 1 hour per response, including the time for reviewing instructions, searching existing data sources, gathering and maintaining the data needed, and completing and reviewing the collection of information. Send comments regarding this burden estimate or any other aspect of this collection of information, including suggestions for reducing this burden, to Washington Headquarters Services, Directorate for Information Operations and Reports, 1215 Jefferson Davis Highway, Suite 1204, Arlington, VA 22202-4302, and to the Office of Management and Budget, Paperwork Reduction Project (0704-0188), Washington, DC 20503.

1. AGENCY USE ONLY (*Leave blank*)

2. REPORT DATE
15 May 2002

3. REPORT TYPE AND DATES COVERED
Quarterly Technical Report, 1 February –30 April 2002

4. TITLE AND SUBTITLE
Solid State Research

5. FUNDING NUMBERS
C — F19628-00-C-0002

6. AUTHOR(S)
David C. Shaver

7. PERFORMING ORGANIZATION NAME(S) AND ADDRESS(ES)
Lincoln Laboratory, MIT
244 Wood Street
Lexington, MA 02420-9108

8. PERFORMING ORGANIZATION REPORT NUMBER
2002:2

9. SPONSORING/MONITORING AGENCY NAME(S) AND ADDRESS(ES)
HQ Air Force Materiel Command
AFMC/STSC
Wright-Patterson AFB, OH 45433-5001

10. SPONSORING/MONITORING AGENCY REPORT NUMBER
ESC-TR-2001-082

11. SUPPLEMENTARY NOTES
None

12a. DISTRIBUTION/AVAILABILITY STATEMENT
Approved for public release; distribution is unlimited.

12b. DISTRIBUTION CODE

13. ABSTRACT (*Maximum 200 words*)

This report covers in detail the research work of the Solid State Division at Lincoln Laboratory for the period 1 February–30 April 2002. The topics covered are Quantum Electronics, Electro-optical Materials and Devices, Submicrometer Technology, Biosensor and Molecular Technologies, Advanced Imaging Technology, Analog Device Technology, and Advanced Silicon Technology. Funding is provided by several DoD organizations—including the Air Force, Army, DARPA, MDA, Navy, NSA, and OSD—and also by the DOE, NASA, and NIST.

14. SUBJECT TERMS
quantum electronics, electro-optical devices, materials research, submicrometer technology, biosensor technology, molecular technology, advanced imaging technology, analog device technology, semiconductor lasers, InGaAsInP p-i-n photodiodes, attenuating phase-shifting mass, near-field imaging at 193 nm, charge-coupled devices, analog array processor, microelectromechanical systems

15. NUMBER OF PAGES
68

16. PRICE CODE

17. SECURITY CLASSIFICATION OF REPORT	18. SECURITY CLASSIFICATION OF THIS PAGE	19. SECURITY CLASSIFICATION OF ABSTRACT	20. LIMITATION OF ABSTRACT
Unclassified	Same as Report	Same as Report	Same as Report

NSN 7540-01-280-5500

Standard Form 298 (Rev. 2-89)
Prescribed by AMSI Std. 239-18
298-102